Correspondence: jingxuan.wei@austin.utexas.edu

Unlocking A Global Ocean Mixing Dataset: toward Standardization of Seismic-derived Ocean Mixing Rates

Jingxuan Wei,[a] Zeyu Zhao,[b] Kathryn L. Gunn,[c] Sean P. S. Gulick,[a,d] Donna J. Shillington,[e] Christopher M. Lowery[a]

[a] *Institute for Geophysics, Jackson School of Geosciences, University of Texas at Austin, Austin, Texas*

[b] *School of Earth and Space Sciences, Peking University, Beijing, China*

[c] *School of Ocean and Earth Science, University of Southampton, Southampton, UK*

[d] *Department of Earth and Planetary Sciences, Jackson School of Geosciences, University of Texas at Austin, Austin, Texas*

[e] *School of Earth and Sustainability, Northern Arizona University, Flagstaff, Arizona*

Corresponding author: Jingxuan Wei, jingxuan.wei@austin.utexas.edu

ABSTRACT

Turbulent mixing is vital for water transformation in the ocean and sustains the global thermohaline circulation. Despite decades of global observations using different platforms, our understanding of ocean turbulence is still limited. More observations are needed to better characterize the spatio-temporal distribution of mixing to reduce uncertainties in climate models. Marine seismic reflection surveys are an untapped data resource for high-resolution ocean turbulence observation. Turbulent mixing can be extracted from seismic data through horizontal internal wave slope spectra. However, to date, a standardized approach to prepare seismic data for this spectral analysis is still lacking, leading to insufficient consideration of the impact of noise on the resulting diffusivities. To address these issues, we perform a full-wavefield synthetic modeling and processing to reveal noise-induced overestimation of diffusivities. We further propose a widely applicable workflow and apply it to three field seismic surveys with increasing noise levels conducted in regions of different turbulence environments: ocean ridges, open ocean interior, and continental slope. The derived diffusivities are benchmarked against direct measurements around the region to show the fidelity of this seismic method. The extended observation records by seismic data across the Kauai Channel and away from Mid-Atlantic Ridges reveal the importance of topography in modifying the propagation of internal tides and the distribution of turbulent mixing in both near and far fields. Our proposed workflow marks a key advancement towards standardization of seismic-derived ocean mixing rates and holds the potential to unlock massive marine seismic reflection dataset worldwide for ocean mixing characterization.

1. Introduction

Ocean turbulence is a fundamental process in transferring momentum and energy between different water masses, facilitating exchanges between the ocean's surface and its depths, thereby maintaining the global overturning circulation. The breaking of internal waves, which irreversibly mixes water across density gradients, serves as the primary driver of turbulence. Observing, analyzing, and modeling turbulent mixing is crucial to understand and predict regional and global climate (MacKinnon et al., 2017). It is widely accepted that an average diapycnal diffusivity (K_ρ) of 10^{-4} m^2 s^{-1} is required to close the global mixing budget (Munk and Wunsch, 1998), yet observations in the open ocean thermocline suggest values one order of magnitude lower (Waterhouse et al., 2014), implying the existence of mixing hotspots elsewhere. Through decades of observations, studies have discovered that enhanced mixing is mostly concentrated under storm tracks (Whalen et al., 2018), along continental margins (Moum et al., 2002; Alford and Munk, 2019), and in the vicinity of complex topography (Polzin et al., 1997; Ledwell et al., 2000). The geography of mixing hotspots reveals that the energy input into the internal wave field primarily comes from tides and winds (Waterhouse et al., 2014).

The conversion of external energy into the internal wave continuum is a complex process. Internal tides are transformed from barotropic tidal currents as they flow over topography (St. Laurent et al., 2001); ocean currents or eddies impinging on small-scale topographic features generates lee waves (Bell Jr, 1975); storms disturbing the base of mixed layer excites near-inertial waves (Gill, 1984; D'Asaro, 1985). All these processes produce internal waves with a wide spectrum of spatial scales and frequencies that can be decomposed into orthogonal modes (Gill, 1982). Low mode internal waves that have larger vertical scales can propagate across ocean basins with larger group velocities (Alford, 2003), whereas high mode internal waves with smaller vertical scales tend to transfer energy near their generation sites (Polzin et al., 1997). The interaction among waves of different modes and their interactions with topography can cascade energy to smaller scales, ultimately leading to energy dissipation through shear and convective instabilities (Whalen et al., 2020). This continually evolving internal wave field leads to prominent spatio-temporal variability of ocean turbulence, which poses a substantial challenge for existing observation efforts to picture a comprehensive, global mixing pattern (Waterhouse et al., 2014; Whalen et al., 2020). In the meantime, climate research calls for increasing observations on the intermittency of turbulence to reduce uncertainties during simulations (Melet et al., 2016; MacKinnon et al., 2017).

The past several decades has witnessed significant progress in observing ocean turbulence, yet further advancements are needed. Vertical microstructure profilers equipped with fast-response thermistors and shear probes are used to directly sample isotropic turbulence on length scales as small as $\sim O(1)$ mm (Schmit et al., 1988; Lueck et al., 2002). Such instruments require sophisticated ship-based operations. To complement existing platforms, microstructure sensors have been installed on autonomous underwater gliders (Peterson and Fer, 2014; Palmer et al., 2015; Rainville et al., 2017), and technological development is paving the way for their potential installation on Argo floats (Roemmich et al., 2019). Nevertheless, direct measurements of mixing remain scarce and are insufficient to constrain the global distribution of turbulence. To address this challenge, fine-scale parametrization has been proposed, which infers the strength of turbulence from internal wave shear or strain spectra on larger vertical length scales of ~O(1-10) m (Gregg, 1989; Polzin et al., 2014). Using conductivity-temperature-depth (CTD) profilers and Argo floats, fine-scale parametrization has revealed reasonable global distribution of turbulent mixing (Whalen et al., 2012; Kunze, 2017; Whalen et al., 2018). However, it has been difficult to benchmark the results of fine-scale parametrization against direct measurements of turbulence due to inconsistent spatio-temporal scales between the two methods (Whalen, 2021). Additionally, more assumptions being adopted by the fine-scale parametrization also lead to larger uncertainties (Polzin et al., 2014).

Recently, mixing rates have been derived from seismic reflection images by analyzing horizontal internal wave spectra on scales of > O(10) m, either directly from the turbulence subrange, or from the internal wave subrange through fine-scale parametrization (Sheen et al., 2009; Holbrook et al., 2013). This method, usually referred to as reflection slope spectra, is one of the research branches of a nascent field known as Seismic Oceanography (SO). SO is an acoustic technique that uses marine seismic reflection surveys to remotely sense the small fluctuations of temperature and salinity, whereby producing high-resolution thermohaline fine structures across the entire water column at spatial resolutions of ~O(10) m (Fig. 1A) (Holbrook et al., 2003). The current development of SO and its distinctive features compared to other observations have been comprehensively reviewed by Dickinson and Gunn (2022).

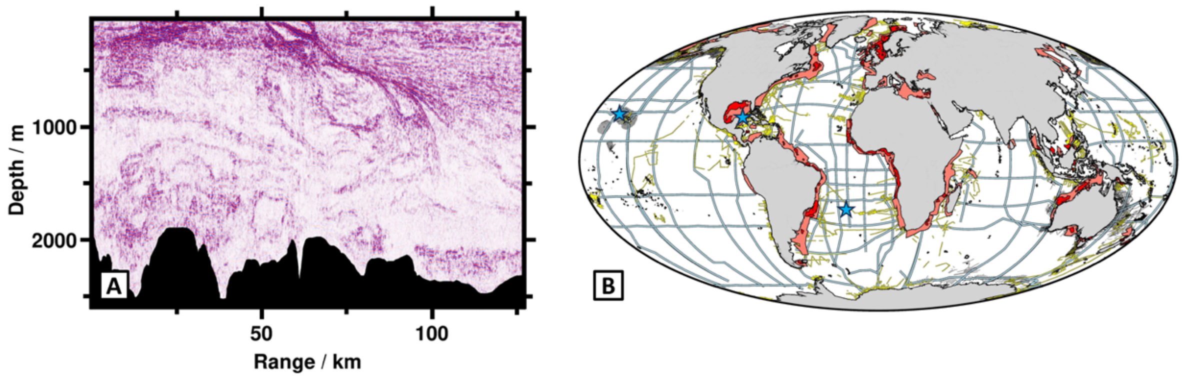

Fig. 1. (A) An example of seismic oceanographic image showing oceanic front at Brazil-Malvinas Confluence. Red colors = positive acoustic amplitudes; blue colors = negative acoustic amplitudes; black region = seafloor. (B) Global coverage of legacy marine reflection seismic data. Dark red polygons = regions covered by three-dimensional surveys acquired by seismic exploration companies; thin black lines = publicly available two-dimensional surveys acquired by seismic exploration companies in other regions; yellow lines = publicly available two-dimensional surveys acquired by research institutions; light blue lines = hydrographic transects of World Ocean Circulation Experiment; blue stars = locations of seismic data used in this study. (A) and (B) are adapted from Fig. 2D and Fig. 4A of Dickinson and Gunn (2022), respectively.

SO has been used to map the spatial distribution of turbulent mixing in diverse environments, including continental margins (Falder et al., 2016; Fortin et al., 2016; Dickinson et al., 2017); ocean ridges (Tang et al., 2021; Tang et al., 2022), oceanic fronts and mesoscale eddies (Tang et al., 2020; Gunn et al., 2021), open ocean interior (Wei et al., 2022) and the Arctic Ocean (Yang et al., 2023). All these studies utilized legacy seismic data acquired by energy industries and academic institutes over the past several decades (Here, we define "legacy" as seismic surveys designed to image the solid Earth instead of the water column). These data exist in abundance, spread across the globe, and can be utilized without incurring additional acquisition expenses (Fig. 1B). For example, Dickinson and Gunn (2022) estimated > 6.3 million km^2 of two-dimensional seismic data and > 5.5 million km^2 of three-dimensional seismic data from five major exploration companies. Exploring legacy seismic data has the potential to yield an unparalleled catalogue of horizontal wavenumber spectra, offering an opportunity to address some fundamental knowledge gaps in downscale energy cascade (Falder et al., 2016; Sallares et al., 2016).

Despite SO's huge potential, several challenges have prevented the method from being accepted by the broader oceanographic community. First, the method lacks a consistent and reliable way to process seismic data, which introduces uncertainties to subsequent analysis. Second, the derived diffusivities have not been benchmarked against direct measurements. To address these problems, a deeper understanding of how seismic data processing impacts spectral analyses and the derived diffusivities is imperative.

Here, we begin by briefly reviewing the principles and current practices used in deriving diapycnal diffusivities from seismic reflection data. We then delve into the immediate challenges encountered in seismic data processing of water column reflections, particularly discussing the issue of low signal-to-noise (S/N) ratios of legacy seismic data. We further demonstrate the susceptibility of reflection slope spectra to noise contamination using a full-wavefield synthetic modeling dataset and propose a workflow to mitigate the low S/N ratio problem. To validate this workflow, we conduct tests on three seismic field datasets characterized by increasing noise levels. These datasets were acquired using different acquisition systems and collected from regions of different turbulence environments: ocean ridges, open ocean interior, and continental slope. The derived diapycnal diffusivities are benchmarked against direct measurements from the Brazil Basin Tracer Release Experiment

(BBTRE) and the Hawaii Ocean Mixing Experiment (HOME) (Polzin et al., 1997; Rudnick et al., 2003). Through these efforts, our work marks a key advancement toward standardization of the reflection slope spectra method, and thereby holds the potential to unlock massive marine seismic dataset worldwide for ocean mixing research.

2. Overview of seismic-derived turbulence mixing rates

a. Seismic images of the ocean

Ocean thermohaline fine-structures can be detected by repeat sampling of consecutive spatial points, e.g., common midpoints (CMP), in the water column by an acoustic source at the ocean surface, e.g., an air-gun. As the emitted signals travel downward and encounter acoustic impedance interfaces, they are reflected, traveling back upward, and are received by a linear array of hydrophones, e.g., a streamer. Acoustic impedance is defined as a product of density with sound speed in a subsurface medium, which is related to the changes of temperature and salinity between water masses. Vertical gradients of temperature and salinity cause vertical contrasts in acoustic impedance which produce reflection coefficients, and the recorded signals are the reflection coefficients convolved with the acoustic source (Fig. 2). Thus, seismic reflection surveying provides maps of the vertical gradients of temperature and salinity, at a scale smoothed by the wavelength of the acoustic source (Ruddick et al., 2009), which is usually around $O(10)$ m. Holbrook et al. (2013) show that seismic reflections can faithfully reproduce isopycnal displacements in a turbulent ocean.

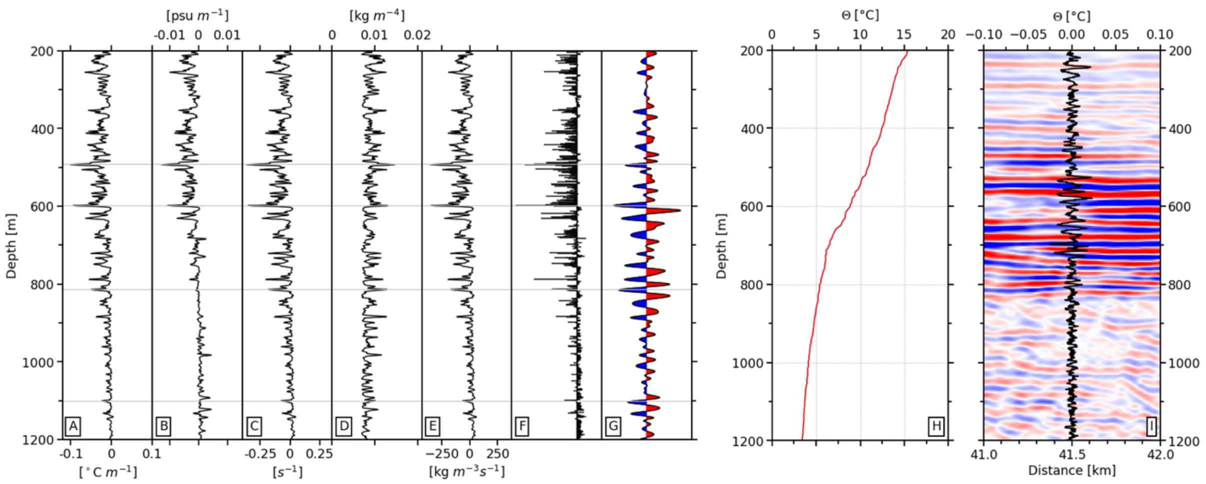

Fig. 2. Vertical gradients of (A) temperature, (B) salinity, (C) sound speed, (D) density, (E) acoustic impedance, and their corresponding reflection coefficients (F). A synthetic seismogram (G) is produced by convolving (F) with a Ricker wavelet. Horizontal grey lines mark the similarities between gradients and synthetic seismogram. The last two panels show

correlation between concurrent XBT and seismic data from the South Atlantic. (H) XBT measured temperature, (I) short wavelength temperature gradients (black line) of the profile in (H) overlie on the seismic section surrounding the collection location of the XBT. Note the correspondence between seismic amplitudes and temperature gradients.

b. Reflection slope spectra

The reflection slope spectra refer to the spectral analysis of vertical displacements of tracked seismic reflections, based on the assumption that seismic reflections follow isopycnals (Krahmann et al., 2009; Holbrook et al., 2013). The basis of this technique is rooted from the horizontal thermistor tow experiments by (Klymak and Moum, 2007a, 2007b), who showed that horizontal isopycnal slope spectra exhibit two distinct subranges that correspond to internal wave and turbulence, each has a slope of -1/2 and +1/3 in log-log space, respectively (Fig. 3A). Moreover, turbulence subrange can extend to surprisingly low wavenumbers, equivalent to horizontal scales exceeding ~500 m (Klymak and Moum, 2007b), far beyond the Ozmidov length scale (10^{-2}-10^{0} m) where isotropic turbulence starts to dominate (Kolmogorov, 1941; Corrsin, 1951; Batchelor et al., 1959). This discovery can be explained by observations and simulations indicating the existence of a regime known as layered anisotropic stratified turbulence (LAST) (Falder et al., 2016). LAST shares the same nonlinear downscale energy cascade as isotropic turbulence and occupies the horizontal scales between internal waves (10^{2}-10^{3} m) and the Ozmidov length scale (Lindborg, 2006; Klymak and Moum, 2007b; Riley and Lindborg, 2008; Kunze, 2019; Caulfield, 2021).

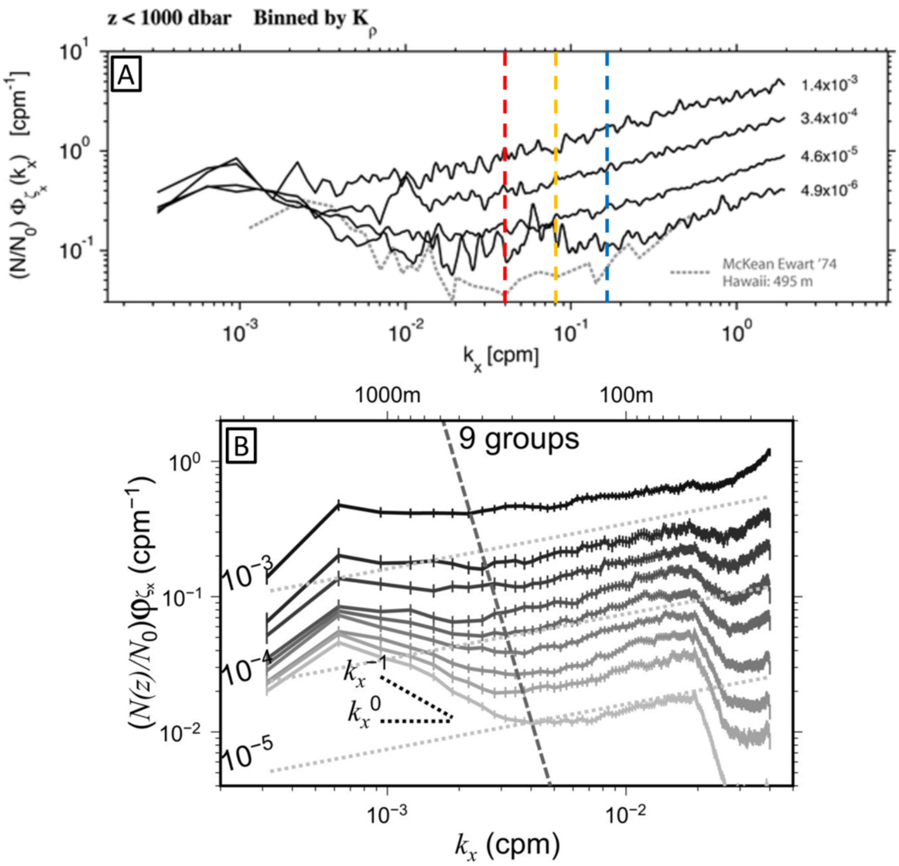

Fig. 3. Slope spectra produced by microstructure and seismic measurements. (A) Average isopycnal slope spectra derived from the Hawaii Ocean Mixing Experiment (HOME). Spectra are binned in one-decade bins of the turbulent diffusivity estimated from shear probe (adapted from Fig. 3 of Klymak and Moum (2007b)). Red, yellow, and blue dashed lines mark the Nyquist wavenumbers of 0.04, 0.08 and 0.16 that are visible to seismic reflection surveys using receiver spacings of 25 m, 12.5 m, and 6.25 m, respectively (corresponding to CMP spacings of 12.5 m, 6.25 m, and 3.125 m). The observable wavenumber ranges suggest that the LAST regime is easily resolved by modern seismic acquisition systems. (B) Average seismic reflection slope spectra derived from seismic data using receiver spacing of 25 m around the Island of Taiwan. Spectra are decomposed by energy level in the turbulence subrange for increments of 0.15 logarithmic units. Vertical black bars represent 95% confidence interval. The dashed gray line shows the migration of the crossover between internal wave and turbulence subrange with respect to spectra energy level. Dotted gray lines in show spectral levels for K_ρ of 10^{-3}, 10^{-4}, and 10^{-5} m^2 s^{-1} (after Fig. 5d of Tang et al. (2022)).

As the horizontal scales of internal waves and LAST are easily resolved by seismic reflection images (Fig. 3), Sheen et al. (2009) presented the first study to estimate turbulent mixing rates from both internal wave and turbulence subranges of reflection slope spectra. The inference of turbulence from the internal wave subrange follows a modified fine-scale parametrization approach which is an indirect estimate of turbulence and is not discussed in this study (e.g., Klymak and Moum (2007a); Dickinson et al. (2017)). In contrast, the turbulence subrange that represents LAST is related to isotropic turbulence through energy cascade and provides an opportunity to directly measure turbulent dissipation ε by fitting to the Batchelor model (Batchelor et al., 1959):

$$\varphi_{\zeta_x}^{T} = \frac{4\pi\Gamma}{N^2} C_T \, \varepsilon^{2/3} \left(2\pi k_x \right)^{1/3} \tag{1}$$

where $\Gamma = 0.2$ is the empirical mixing efficiency (Osborn and Cox, 1972), N is buoyancy frequency, $C_T = 0.4$ is the Kolmogorov constant, and k_x is horizontal wavenumber. Diapycnal diffusivity, K_ρ, is then calculated using the Osborn relationship (Osborn, 1980):

$$K_\rho = \Gamma \varepsilon / N^2 \tag{2}$$

Dickinson et al. (2020) and Tang et al. (2021) have assessed the uncertainties of seismically derived diffusivities. The major uncertainty comes from the fitting of the slope spectrum to the Batchelor model, which can be represented by the following relations:

$$\begin{cases} b = \dfrac{1}{M} \sum_{i=1}^{M} \left(\log_{10} \varphi_{\zeta_x,i}^{T} - \dfrac{1}{3} \log_{10} k_{x,i} \right) \\ \varepsilon(b) = \dfrac{N^3}{4\pi^2} \left(\dfrac{10^b}{2 C_T \Gamma} \right)^{3/2} \\ \sigma_b = \left[\dfrac{1}{M} \sum_{i=1}^{M} \left(\log_{10} \varphi_{\zeta_x,i}^{T} - \dfrac{1}{3} \log_{10} k_{x,i} - b \right)^2 \right]^{1/2} \\ \varepsilon^{\pm} = \varepsilon\left(b \pm \sigma_b \right) \end{cases} \tag{3}$$

Where $\varphi_{\zeta_x,i}^{T}$ is the slope spectrum value corresponding to wavenumber $k_{x,i}$ within the turbulence subrange, M is the number of $k_{x,i}$ in the turbulence subrange, b is the intercept of the fitted straight line in $\log_{10}(k_x) - \log_{10}(\varphi_{\zeta_x,i}^{T})$ space, σ_b is the standard deviation of the residual fitting, $\varepsilon(b)$ represents dissipation rates as a function of b, and $\varepsilon^{\pm}$ means the upper and lower bounds of dissipation rates corresponding to $b \pm \sigma_b$. Other uncertainties come from the choices of N, C_T, and Γ. Both the Kolmogorov constant $C_T = 0.4$ and the mixing coefficient $\Gamma = 0.2$ will introduce uncertainties of ~0.15 logarithmic units in $\log_{10}(K_\rho)$ by taking the upper and lower bounds of their observed ranges of $C_T \in [0.3, 0.5]$ and $\Gamma \in [0.1, 0.4]$, respectively. The uncertainties introduced by N are minor and subject to change dependent on local hydrographic conditions. In this study, we follow this criterion and uncertainties from each contributing factors are specified in section 5.1.

The isopycnal slope spectra of Klymak and Moum (2007b) and reflection slope spectra share similar characteristics. First, the rise and fall of spectra energy levels with respect to turbulent mixing rates is evident in both spectra (Fig. 3). Second, the crossovers between internal wave and turbulence subranges in both spectra migrate to lower wavenumbers as spectra energy increase, indicating LAST extending to greater horizontal scales where stronger internal waves propagate (Fig. 3). These similarities support the reliability of reflection slope spectra in capturing the intensity of internal waves and turbulence. Therefore, this technique has been frequently used to study turbulent mixing in various environments (Song et al., 2021). However, different from thermistor tow measurements, seismic imaging does not directly measure temperature variations. It requires a series of data processing to convert the acoustic signals to final seismic images. Uncertainties can rise from noise contamination and different seismic processing techniques being used, and eventually propagate into the derived turbulent mixing rates. Here we examine this long-standing issue and propose a generic solution for future applications.

c. Data preparation

Seismic Oceanography needs meticulous data processing as the seismic reflectivity of the water column is about 10^2-10^3 times weaker than the solid Earth. Therefore, special care is needed to minimize the effect of noise in modifying the shapes and energy levels of the reflection slope spectra. For example, Holbrook et al. (2013) systematically explored how noise can affect slope spectra analysis. First, they found that the harmonic noise, stemming from the periodic change of seismic amplitudes due to the move-up rate of the seismic acquisition, i.e., the number CMPs generated per shot, can create a spurious turbulence subrange. Second, they discussed the significance of S/N ratio and proposed the application of a band-pass filter for random noise attenuation. Subsequent studies have generally followed this workflow to derive diapycnal diffusivities (Falder et al., 2016; Fortin et al., 2016; Dickinson et al., 2020; Tang et al., 2020). Yet, band-pass filter is usually insufficient for effectively suppressing random noise (Fig. 4A). Noise that shares the same frequency range with reflections can persist. In particular, this workflow overlooks an important source of noise in seismic oceanography: previous shot multiples.

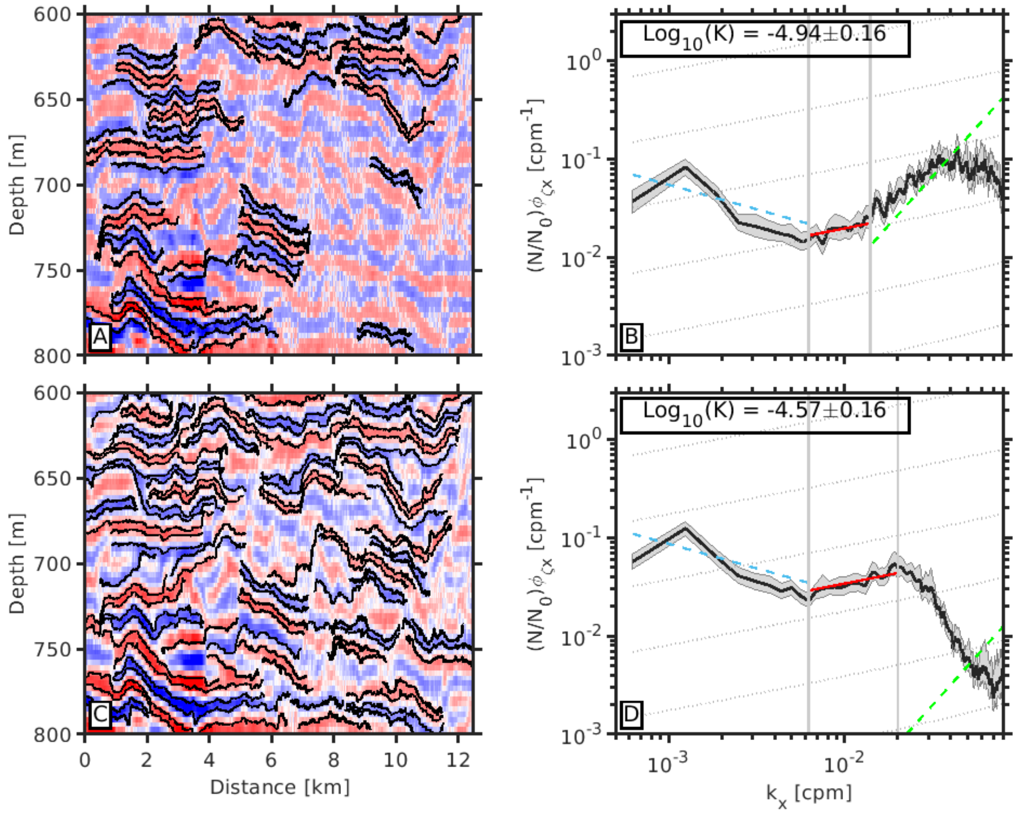

Fig. 4. Example spectra analysis of legacy marine seismic data at the Hawaiian Ridge (Fig. 5B). (A) Tracked reflections overlay on band-pass filtered seismic data with S/N ratio of 5.5, satisfied the criterion of S/N ratio of 4 by Holbrook et al. (2013). (B) Average reflection slope spectrum calculated from tracked reflections in (A). (C) Same data in (A) but smoothed by a Gaussian filter with standard deviation of 1. (D) Average reflection slope spectrum calculated from tracked reflections in (C). Shaded gray area = 95% bootstrap confidence intervals. Dashed blue lines ($k_x^{-1/2}$), solid red lines ($k_x^{1/3}$) and dashed green lines (k_x^{2}) = the internal wave subrange, turbulence subrange and white noise, respectively (Garrett and Munk, 1975; Klymak and Moum, 2007b; Holbrook et al., 2013). Dashed gray lines = slopes of +1/3 corresponding to diffusivities increasing by one order of magnitude from 10^{-7} to 10^{-2} m^2 s^{-1}. Two vertical gray lines bound the turbulent subrange used to calculate diffusivity. The calculated diffusivities and their uncertainties are shown in the upper left corner. In this example, uncertainties only account for errors in buoyancy frequency and straight-line fitting.

Previous shot multiples are strong reverberations bouncing between the seafloor and the sea surface generated by previous shots. Their appearances in the acoustic records are functions of ocean depth, shot spacing and seafloor composition. Deeper ocean depths, smaller shot spacing, and harder seafloors (higher reflection coefficient) favor the generation of previous shot multiples (Fig. 5D). They overprint water column reflections as coherent noise with inconsistent arrival times across shot gathers but become "random" after CMP sorting and stacking. However, due to their strong amplitudes relative to reflections from water column arrivals, stacking is not sufficient to suppress them. This issue is particularly problematic for legacy marine seismic data whose acquisition geometry were originally designed to image the solid Earth.

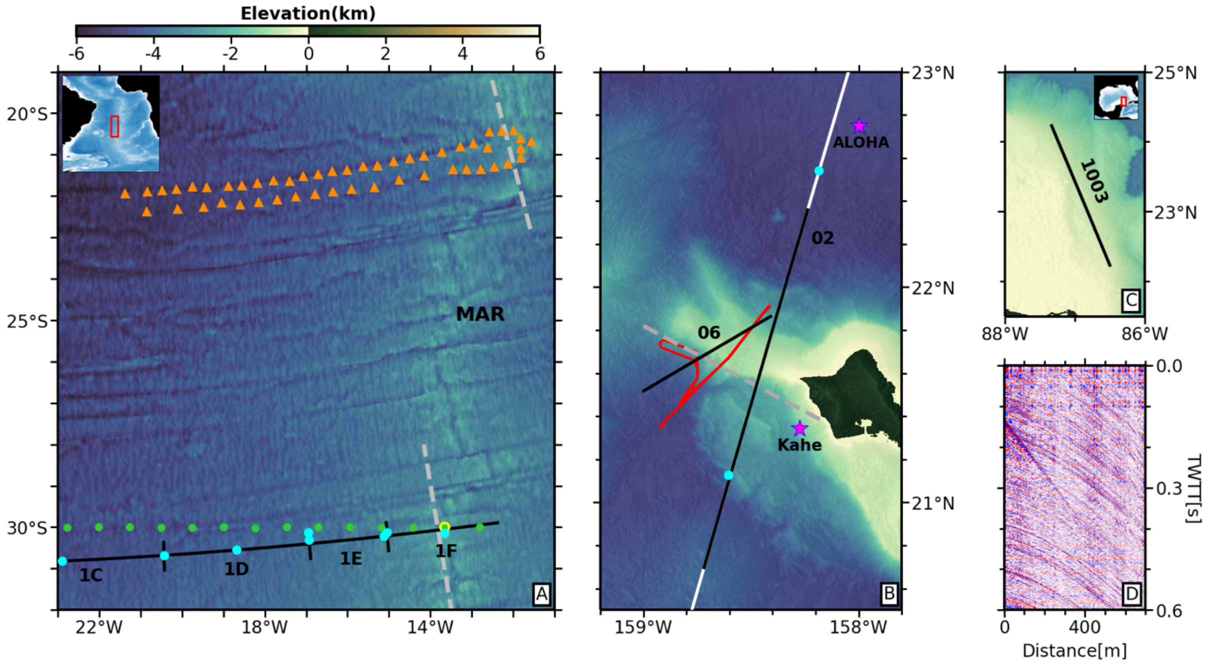

Fig. 5. (A) Bathymetric map of the central South Atlantic where the CREST seismic survey and the BBTRE microstructure profilers were collected. Black lines = CREST seismic lines; green dots = CTD casts from GO-SHIP survey, the one with yellow edge is used to build the synthetic turbulence model in section 4.1; cyan dots = XBTs collected during the seismic survey; orange triangles = locations of BBTRE profilers; dashed grey lines = mean axes of the local mid-ocean ridges. (B) Bathymetry map of the Kauai Channel. Black lines = seismic lines 02 and 06 acquired by the Hawaii Experiment, white line = remaining portion of line 02 (not used); red line = trajectory of the Marlin tow by HOME; cyan dots = XBTs coincident with the seismic survey; purple stars = Kahe and ALOHA stations maintained by the Hawaii Ocean Time-series project; dashed grey lines = along ridge direction by Klymak et al. (2006). (C) Bathymetry map of the eastern Campeche Bank. Black line = seismic line 1003 acquired by the Campeche Experiment. (D) Example of a band-pass filtered shot gather from the (C) showing a series of strong, successive previous shot multiples. Insets show large scale geography, with red boxes marking the locations of the study areas. Bathymetry data is from the Global Multi-Resolution Topography Synthesis (Ryan et al., 2009).

Without proper noise attenuation, the turbulence subrange of the slope spectra will be dominated by noise (Fig. 4A, 4B), some might not exhibit a turbulence subrange at all. For legacy seismic data, this implies that certain sections of a seismic line may be suitable for slope spectra analysis while others may not (Holbrook et al., 2013). This issue is usually mitigated by applying a smoothing filter on the final seismic image before slope spectra analysis (Fig. 4C, 4D), as adopted by Holbrook et al. (2013), Fortin et al. (2017), and Tang et al. (2020). Although smoothing can recover turbulence subrange, it is a crude approach that affects the true amplitudes of the seismic reflections and remove the high wavenumber contents of the slope spectra, creating spectra roll-off that adversely affect the fitting accuracy of turbulence subrange (Figs. 3B, 4B). Most importantly, the derived diffusivities are subjected to change before and after smoothing (Fig. 4B, 4D), implying uncontrollable uncertainties are introduced during this process. Therefore, it is vital to investigate this problem and develop a standard way to derive turbulent mixing rates, minimizing uncertainties during seismic data processing.

3. Data

a. Seismic data and processing

A standardized strategy requires universal application to different types of datasets. In this study, we explore two popular seismic acquisition systems that are widely used in both academic and industry. The first system comprises a low frequency (e.g., 5-120 Hz) air-gun array as the acoustic source and a long hydrophone streamer (e.g., 6-15 km), usually with 12.5-m receiver spacing, as the recording cable. The powerful source and wide recording aperture enable imaging of deep subsurface structures such as ocean crust, ridges, seamounts and subduction zones (Gulick et al., 2008; Gulick et al., 2013; Shillington et al., 2015; Estep et al., 2019; Carbotte et al., 2020). These types of surveys are carried out on specialized research vessels equipped with this kind of system, like the R/V *Marcus G. Langseth* in the US Academic Research Fleet who has been collecting high-quality seismic data around the globe.

The second system uses high frequency (e.g., 40-300 Hz) Generator-Injector (GI) air-gun and a relatively short hydrophone streamer (e.g., 75-2000 m) with 3.125- or 6.25-m receiver spacing depending on different configurations. The high frequency bandwidth produces high-resolution images of the subsurface that can be used to study the detail stratigraphy of sediments (Lowery et al., 2024b) or storage of methane hydrates (Serov et al., 2017). The portability of the GI gun system facilitates its deployment across vessels of different sizes and alongside with other oceanographic sensors, making it a promising system for future dedicated seismic oceanographic cruises (Ruddick, 2018).

In this study, we derive diapycnal diffusivities from three seismic datasets collected by the acquisition systems mentioned above during three independent scientific cruises in regions of different turbulence levels:

1) The Crustal Reflectivity Experiment Southern Transect (CREST) experiment, conducted between January and February of 2016 aboard the R/V *Marcus G. Langseth* (Reece and

Christeson, 2017). The primary goal of the CREST survey was to investigate the evolution of oceanic crust at 30° S. The survey spans the eastern edge of the Rio Grande Ridge to the Mid-Atlantic Ridge, including a 1,600-km-long continuous east-west data transect (Fig. 5A). Diffusivities derived from this dataset are compared with the Brazil Basin Tracer Release Experiment (BBTRE) as they both span from the Mid-Atlantic Ridge to the ocean interior (Polzin et al., 1997) (Fig. 5A).

2) The Hawaiian-Emperor Seamount Chain Seismic Experiment (Part 1) (hereafter, Hawaii Experiment), also carried out by R/V *Marcus G. Langseth* from September to October 2018 around the Hawaiian Islands (Shillington et al., 2019) (Fig. 5B). The cruise objective was to examine controls on magmatic addition along the Hawaiian-Emperor seamount chain, to provide fundamental constraints on rheological properties of oceanic lithosphere (Watts et al., 2021). We only use two seismic lines from this survey collected within the Kauai Channel because they were collocated with the Marlin tow microstructure measurements by the Hawaii Ocean Mixing Experiment (HOME) (Klymak et al., 2006) (Fig. 5B).

3) The Campeche Bank Stratigraphy Seismic Experiment (hereafter, Campeche Experiment) took place onboard the R/V *Justo Sierra* in July 2022 (Lowery et al., 2024a), using the Scripps Institute of Oceanography's high-resolution portable multichannel seismic system (Fig. 5C). Its purpose was to map the history of the sediment drift on the eastern Campeche Bank to study the stratigraphic expression of the Loop Current (Lowery et al., 2024b). The water column data of this survey were severely contaminated by previous shot multiples due to short shot spacing (Fig. 5D). Thus, these data provide an opportunity to test the applicability of the proposed processing sequence on very noisy dataset.

Seismic data were processed following a traditional seismic oceanographic procedure for turbulence analysis (Holbrook et al., 2013): geometry definition, direct arrival removal, noise attenuation, CMP sorting, velocity analysis, stacking, amplitude correction, migration, and harmonic noise suppression. As will show in the following sections, this processing flow is not sufficient to accurately derive diffusivities from seismic data and so an additional processing step, the F-K filter, was applied. Detailed acquisition and processing parameters of the three surveys are shown in Table 1.

Survey	CREST Experiment	Hawaii Experiment	Campeche Experiment

Acoustic source	36 bolt air-gun array with a total volume of 6,600 in^3	36 bolt air-gun array with a total volume of 6,600 in^3	2 GI air-gun array with a total volume of 90 in^3
Shot spacing	37.5 m	62.5 m	12.5 m
Number of receiver channels	1008	1200	120
Channel group spacing	12.5 m	12.5 m	6.25 m
CMP spacing	6.25 m	6.25 m	3.125 m
Channel used	600	600	120
Bandpass filter	30-80 Hz	30-80 Hz	40-320 Hz

Table 1. Acquisition and processing parameters of the CREST, Hawaii, and Campeche experiments.

b. Hydrographic data

The derivation of diapycnal diffusivity requires measurements of buoyancy frequency. In the central South Atlantic, the GO-SHIP program collected CTD measurements along the 30° S transect in October 2011 (CCHDO, 2023), which is collocated but not concurrent with the CREST seismic survey (Fig. 5A). From these CTD profiles, we selected 14 profiles that are within the region of analysis and calculate a local mean buoyancy frequency profile for this region using the adiabatic leveling method (Bray and Fofonoff, 1981) (Fig. 6A). Near Oahu, the Hawaii Ocean Time-series (HOT) project maintained by University of Hawaii has been acquiring continuous hydrographic data over the years at stations Kahe and ALOHA (Fig. 5B). We used 26 CTD profiles that were concurrent with the Hawaii seismic experiment collected from September to October 2018 to calculate in-situ buoyancy frequency profiles (Fig. 6B). These depth varying buoyancy profiles, N(z), are used to estimate diapycnal diffusivity for each reflection. We used a constant buoyancy profile of 2.5 cph for the Campeche data because it is used as a test set and there are no direct measurements of turbulence to serve as benchmarks.

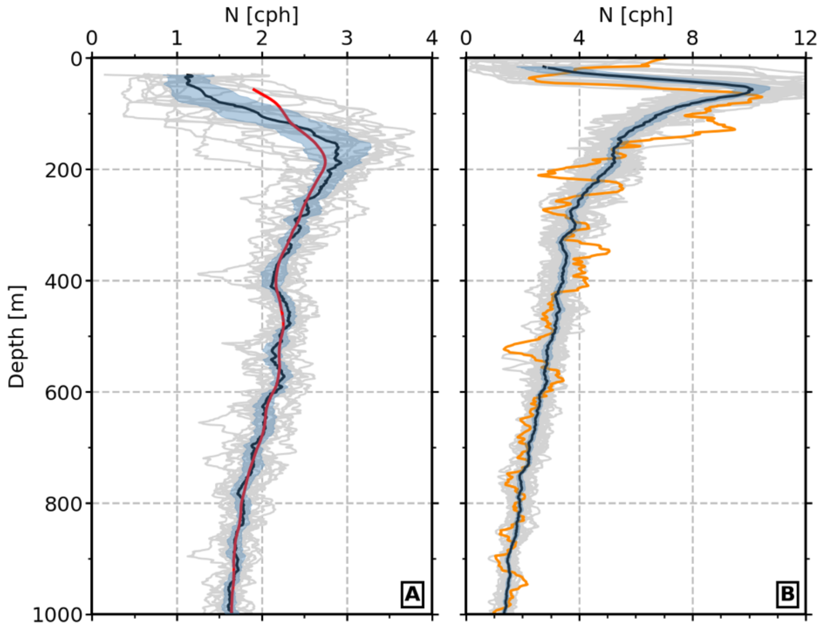

Fig. 6. Buoyancy frequency (*N*) profiles calculated from GO-SHIP CTDs (A) and HOT CTDs (B). Black lines = average profiles; grey lines = individual profiles; blue shades = 95% confident interval; red line = local mean profile calculated using the adiabatic leveling method (Bray and Fofonoff, 1981); orange line = an example profile from station Kahe showing stratification close to the Oahu Island.

4. Susceptibility of reflection slope spectra

a. Synthetic modeling

To assess how noise and seismic data processing affects the derived diffusivities, we performed a full-wavefield simulation across a synthetic sound speed and density model containing spectra characteristics of internal waves and turbulence. The model was created the same way as Holbrook et al. (2013) by using vertical displacements instead of physical modeling of fluid dynamics. Internal wave displacements that governed by Garrett-Munk (GM) spectrum and turbulence that represented by the Batchelor spectrum are independently programmed into the model (Batchelor et al., 1959; Garrett and Munk, 1975). Sound speed and density data is calculated from one of the CTD casts of the GO-SHIP A10 survey (Figs. 5A, 7A). We repeated this sound speed and density profile at 2-m intervals for 20 km and displaced each value by a vertical displacement specified by the GM and Batchelor model. Lastly, the displaced sound speed and density sections are interpolated onto a constant depth interval of 1 m (Fig. 7B).

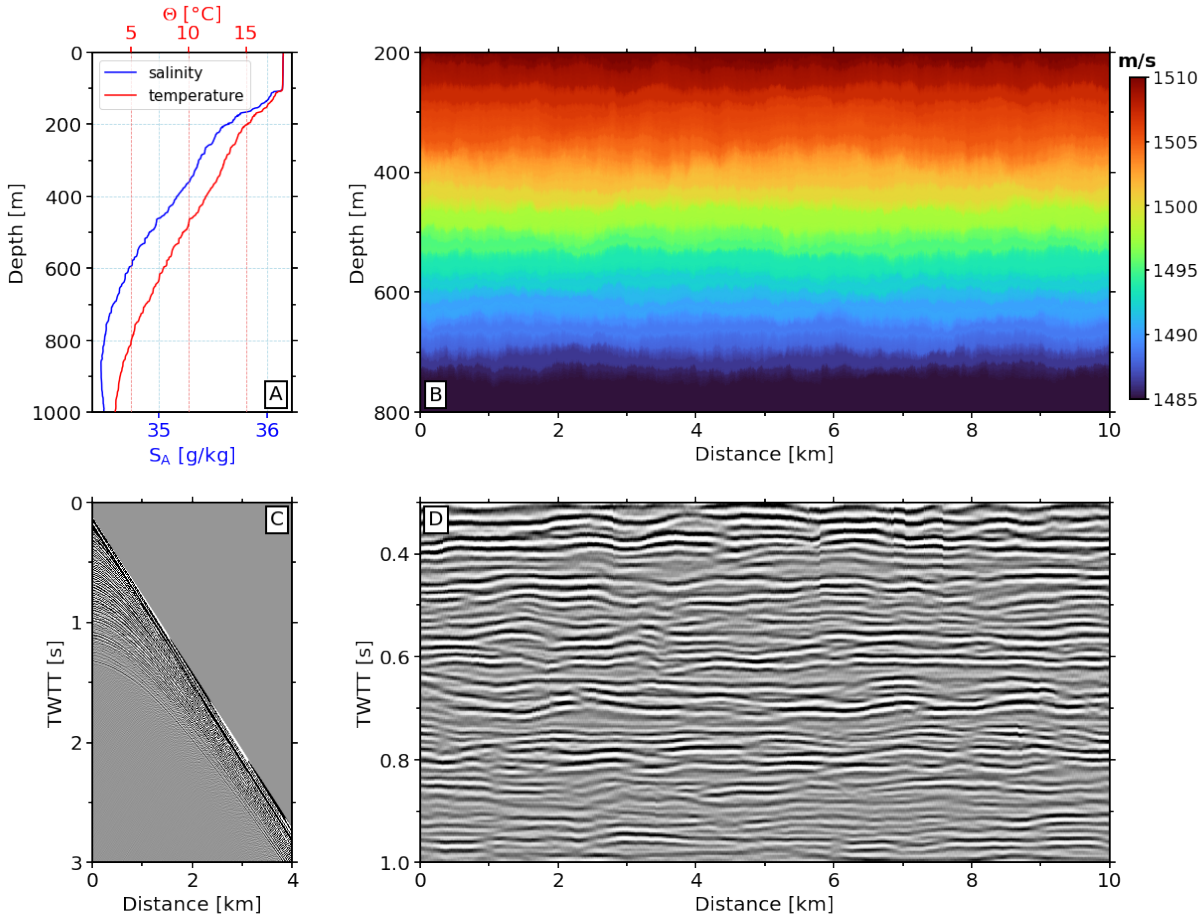

Fig. 7. Full wavefield synthetic modeling. (A) Temperature and salinity profiles from the GO-SHIP CTD above the Mid-Atlantic Ridge as shown in Fig. 5A. (B) Sound speed section created using (A) by applying displacement that simulate the spectra characteristics of internal waves and turbulence. (C) Example of a synthetic shot gather. (D) Final synthetic seismic section.

Different from Holbrook et al. (2013) who used "exploding reflector" sources, we did a full wavefield simulation where seismic waves propagate across the model space. A variable density and velocity seismic forward modeling engine was used to perform the simulation. We employed a set of first order differential equations for particle velocity and stress components (Graves, 1996); and staggered-grid finite difference method was used to numerically solve the wave propagation with 6th order spatial derivatives and 2nd order temporal derivative.

We simulated a marine seismic acquisition system with 600 receivers spaced 12.5 m apart towed on the left side of the shot positions. A very small shot spacing of 6.25 m was used to increase the horizontal sample rate to capture the non-physical displacements of internal waves and turbulence in the model space. More realistic physical modeling is needed in the future to examine the capabilities of normal shot spacing (e.g., 37.5 m in the CREST survey) in detecting internal waves and turbulence signatures. A Ricker wavelet with 50 Hz main frequency is used for the wave propagation. Both source and receivers are placed at a depth of 12m below the horizontal sea surface. A total of 1965 shots were simulated with recording length of 4 s and sample interval of 0.5 ms (Fig. 7C). We then carried out pre-stack and post-stack processing to produce a noise free synthetic seismic section. Processing steps includes CMP sorting, velocity analysis, stacking and migration. Velocity analysis was performed on each CMP gather to capture the artificial displacements of internal waves and turbulence. The final seismic section is 10 km long and contains equal levels of turbulence everywhere (Fig. 7D). The synthetic seismic section and shot gathers are used to investigate the effect of noise and data processing on reflection slope spectra.

b. Impact of noise and smoothing filter

As discussed above, noise is an unresolved issue for reflection slope spectra. Moreover, the side-effects of the frequently used smoothing filter have not been well studied. Here, we use the synthetic seismic section (Fig. 7D) to explore these issues by testing four scenarios: (a) the original noise-free synthetic section; (b) smoothed noise-free section: data in (a) are smoothed by a Gaussian smoothing kernel with standard deviation of 0.5; (c) noise-added section, random noise generated by the MATLAB randn function is added to data in (a). (d) smoothed noise-added section, the data in (c) are smoothed using the Gaussian smoothing kernel with standard deviation of 1. We derived diapycnal diffusivities using the average slope spectrum calculated from the tracked reflections of each section (Fig. 8). The results of each scenario are listed below:

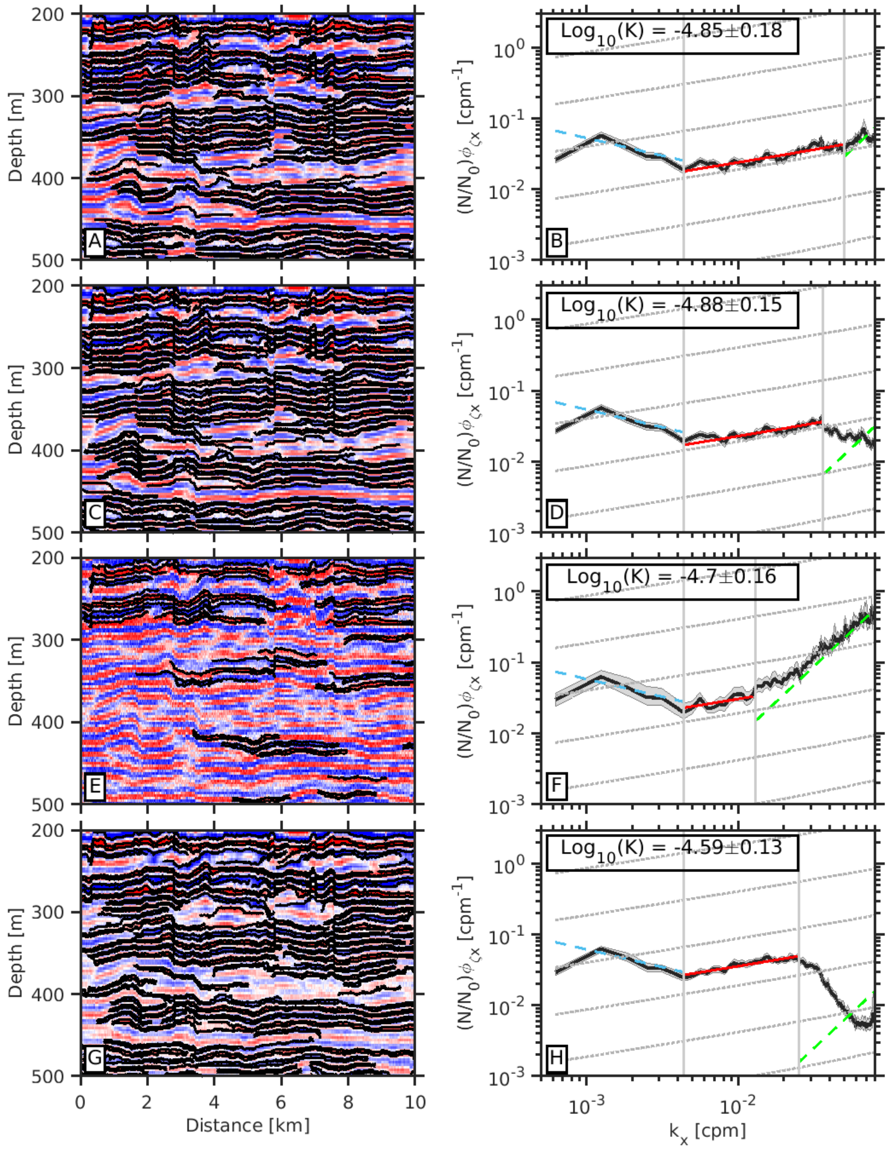

Fig. 8. Demonstration of the noise test on the synthetic seismic section. (A) Noise-free section with tracked reflections. (B) Average slope spectrum calculated from tracked reflections in (A). (C-D), (E-F), (G-H) Same as (A-B) but for smoothed noise-free section, noise-added section, and smoothed noise-added section, respectively. Uncertainties of diffusivities only account for errors in buoyancy frequency and straight-line fitting. Color scheme same as in Fig. 4.

a) Noise-free section: the average slope spectrum shows an interval wave subrange with -1/2 slope and a turbulence subrange with +1/3 slope, the crossover between the two is at wavenumber 0.004375 cpm (Fig. 8B). A pseudo noise subrange appears at wavenumbers higher than 0.05 cpm which is caused by the modeling artifact (Fig. 8B).
b) Smoothed noise-free section: The smoothing causes a spectrum roll-off after 0.036 cpm and slightly lowered the diffusivity by 0.03 logarithmic units from -4.85 to -4.88,

comparing with the first scenario (Fig. 8D). Stronger smoothing (e.g., using higher standard deviation) can further erode the turbulence subrange but do not significantly alter the diffusivity values.

c) Noise-added section: It is evident that noise disrupts the continuity of seismic reflections, resulting in fewer reflections being tracked and used when calculating the average spectrum (Fig. 8E). In the spectrum, a large portion of turbulence subrange is dominated by noise, creating a noise subrange with +2 slope after 0.013 cpm (Fig. 8F). Notably, the derived diffusivity increased significantly by 0.18 logarithmic units compared with the first case, which is also reflected in the elevation of the energy level of the spectrum.

d) Smoothed noise-added section: Smoothing increases S/N ratio and enabled tracking of more reflections (Fig. 8G). A longer turbulence subrange is recovered in the wavenumber range of 0.004375-0.025 cpm (Fig. 8H). The derived diffusivity increases by 0.11 logarithmic units from -4.7 to -4.59 compared with the third case.

By comparing results between the four scenarios, the following conclusions can be drawn. First, smoothing filter itself does not significantly change the derived diffusivities except eroding away turbulence subrange at higher wavenumbers. Second, the presence of noise increases the energy level of the spectrum at wavenumbers pertained to turbulence subrange and can lead to overestimation of the derived diffusivity. Lastly, smoothing a noisy dataset worsen the overestimation, likely due to the superposition of spectrum energy that comes from noise onto the spectrum energy from vertical displacements. Therefore, to accurately derive mixing rates from seismic data, it is advisable to suppress noise as much as possible.

5. A spectral solution

a. F-K filter

Through our investigation into the impact of noise, we find that the weaker the noise the more accurate the derived diffusivities. One of the strongest sources of noise comes from previous shots multiples that have usually been neglected due to their random distribution of arrival times across shot gathers. Although they are added de-constructively during stacking, their high amplitudes relative to water column reflections leave considerable residual noise in the final seismic section. Furthermore, simple frequency filtering failed to remove these multiples since they share the same frequency range with reflections. However, it is possible to separate them in shot gathers prior to stacking.

In a geometric sense, without considering higher accuracy at far offsets, a single reflection in a shot gather (time-distance domain) is approximated as a hyperbola:

$$t^2 = t_0^2 + \frac{x^2}{v^2} \tag{4}$$

where t is the reflection traveltime, t_0 is the two-way-traveltime at normal incidence, x is the distance (offset) between the source and receivers, v is the velocity of the medium above the reflecting interface (Yilmaz, 2001). In the meantime, the entire recorded wavefield in a shot gather can be treated as a synthesis of many plane waves with different dips and are separable through two-dimensional Fourier transform:

$$\begin{gathered} F(f,\ k) = \iint \mathrm{f}(t,\ x)\, exp\left[(-j2\pi(ft + kx))\right] dtdx \\ \mathrm{f}(t,\ x) = \iint F(f,\ k)\, exp\left[j2\pi(ft + kx)\right] df\, dk \end{gathered} \tag{5}$$

where f(t, x) represents time-space domain and F(f, k) represents frequency-wavenumber domain. Seismic events in the two domains can be related through apparent velocities (dips), $V_{app} = dx/dt = df/dk$. In other words, events with the same dip in the $t-x$ domain, regardless of location, are mapped onto a single line in the radial direction in the $f-k$ spectrum (Fig. 9) (Details of 2D Fourier transform in seismic data can be found in Chapter 3 of Yilmaz (2001)). Since previous shot multiples do not exhibit the same hyperbolic shapes as they are reflected multiple times between the seafloor and sea surface, resulting in significantly smaller curvatures compared to reflections (Fig. 10A). Therefore, we can separate reflections from multiples based on their curvature differences (dip differences).

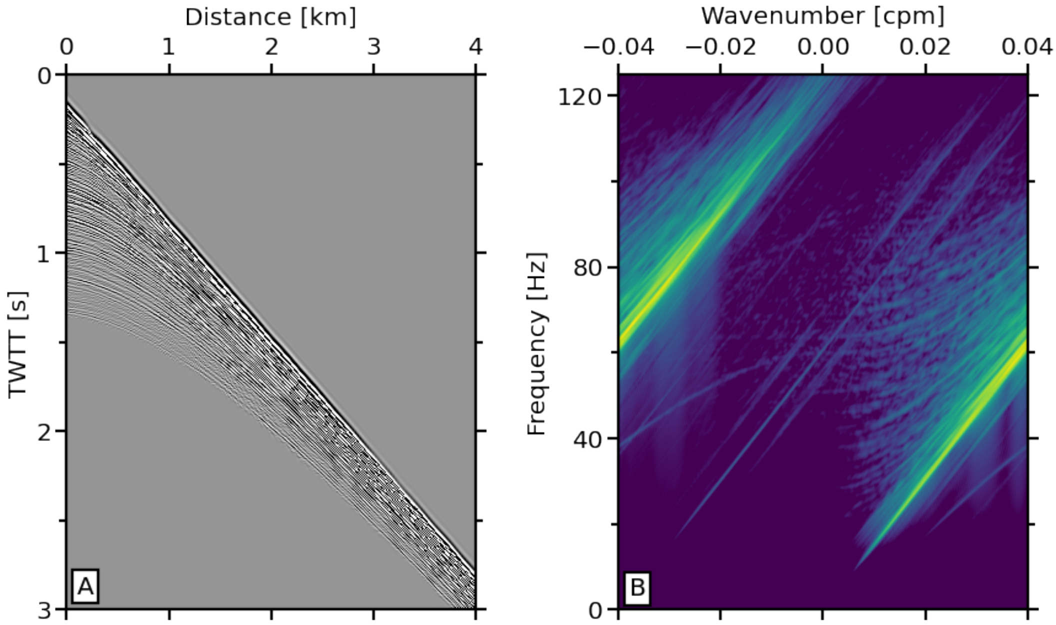

Fig. 9. A synthetic shot gather with direct arrival removed (A) and its F-K spectrum (B).

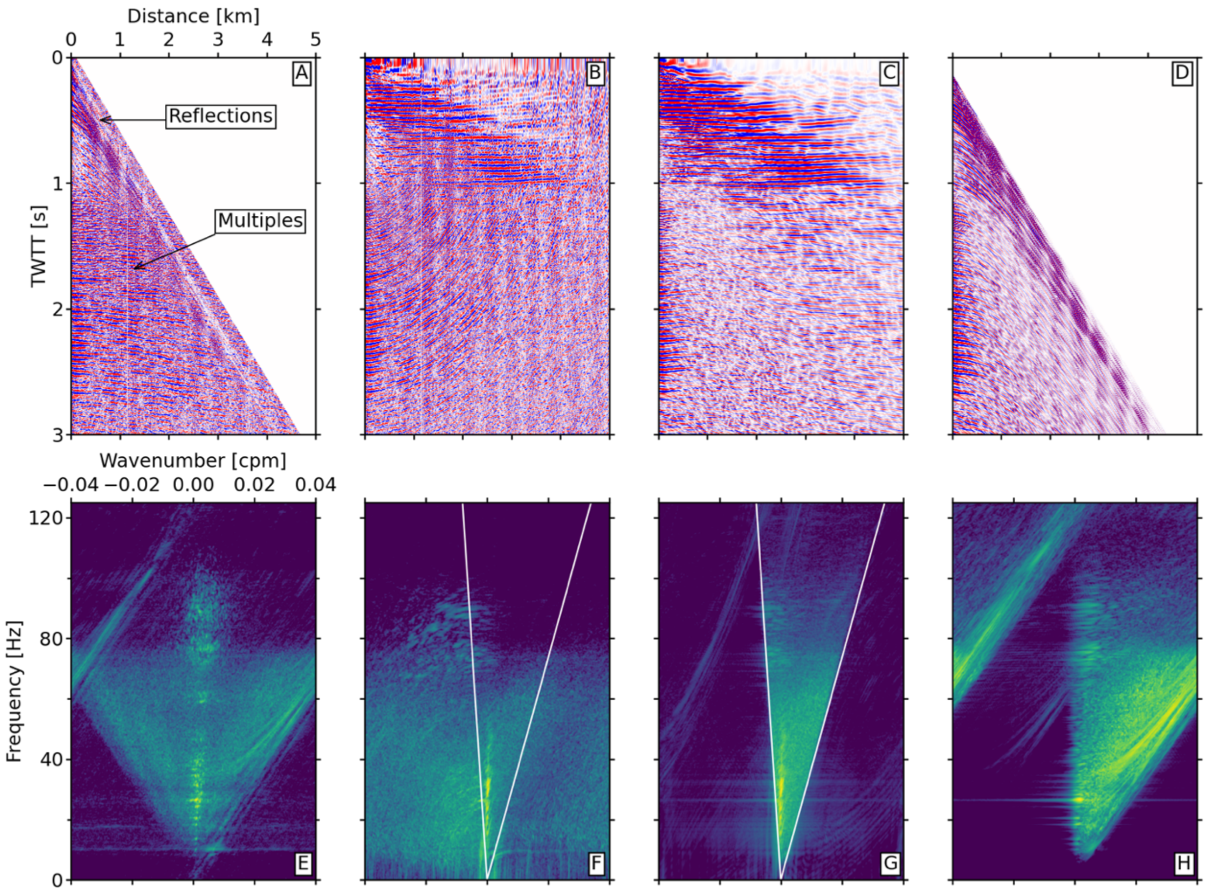

Fig. 10. Steps of F-K filter on a shot gather with direct arrival removed from the Hawaii Experiment. (A) Input shot gather, note the overprint of multiples onto reflections at distance > 1 km. (B) NMO correction applied. (C) F-K filter applied. (D) NMO correction removed. (E-

H) Corresponding F-K spectra of data in (A-D). White lines in (F) and (G) represent the fan-shape dip filter.

F-K filter, or dip filter, is a proven technique in reflection seismology to remove coherent noise such as ground rolls and guided waves in the $f - k$ domain (Yilmaz, 2001). With proper data preparation, we design a processing sequence that utilizes F-K filter to remove previous shot multiples from the water column. Taking a band-pass filtered (30-80 Hz) shot gather from the CREST survey as a demonstration (Fig. 10), the processing sequence includes four steps:

1) Determine a velocity model for shot gathers. The model can be built through the same interactive velocity analysis applied to CMP gathers. However, unlike the velocity model used for stacking, it does not require the same level of detail since it is only used to roughly flatten reflections. For instance, velocities can be picked every 1000 shots. If the hydrographic properties remain relatively consistent along the seismic transect, a 1D velocity model may suffice. In this study, we used the velocities measured by coincident XBTs (Fig. 5).
2) Apply normal-moveout (NMO) correction using the created velocity model to flatten water column reflections while over-correcting previous shots multiples, causing them to dip/curve upward (Fig. 10B). Through this process, multiples are mapped onto the negative wavenumber quadrant in the F-K spectrum while reflections gather around 0 wavenumber along the frequency axis, forming a vertical stripe of high spectra energy (Fig. 10F). The application of NMO on shot gathers assumes that reflectors in the water column have gentle dipping angles, which this is usually true as the thermohaline structures rarely dip greater than 10° (Sheen et al., 2011).
3) Design a F-K filter to remove coherent noise. Because of the redundancy inherent in the Fourier transform, it is permissible to eliminate much of the spectra energy in the negative wavenumber quadrant that corresponds to previous shot multiples, retaining only the energy centered around zero wavenumber. Here, we follow Yilmaz (2001) to define the F-K filter in ms/trace. As shown in Fig. 10G, a fan-shape dip filter starting from the origin, spanning between -1 and 3.5 ms/trace is applied to remove multiples and further reduce random noise. The reason to partially remove energy in the positive wavenumber quadrant is discussed in the next section.
4) Apply inverse NMO correction with the same velocity model in step (1) to restore reflections to original positions. It is recommended to follow up with a band-pass filter

to remove artifacts resulted from the inverse transform of spectra discontinuities in the F-K domain.

We applied this processing strategy to the Campeche experiment which is severely contaminated by multiples due to fine shot spacing (Fig. 5D). As shown in Fig. 11, previous shot multiples are effectively removed without harming the amplitudes of water column reflections. Additionally, a substantial amount of water column structure, previously obscured or masked by noise, have now been recovered, suggesting the advantages of noise attenuation in pre-stack processing stages.

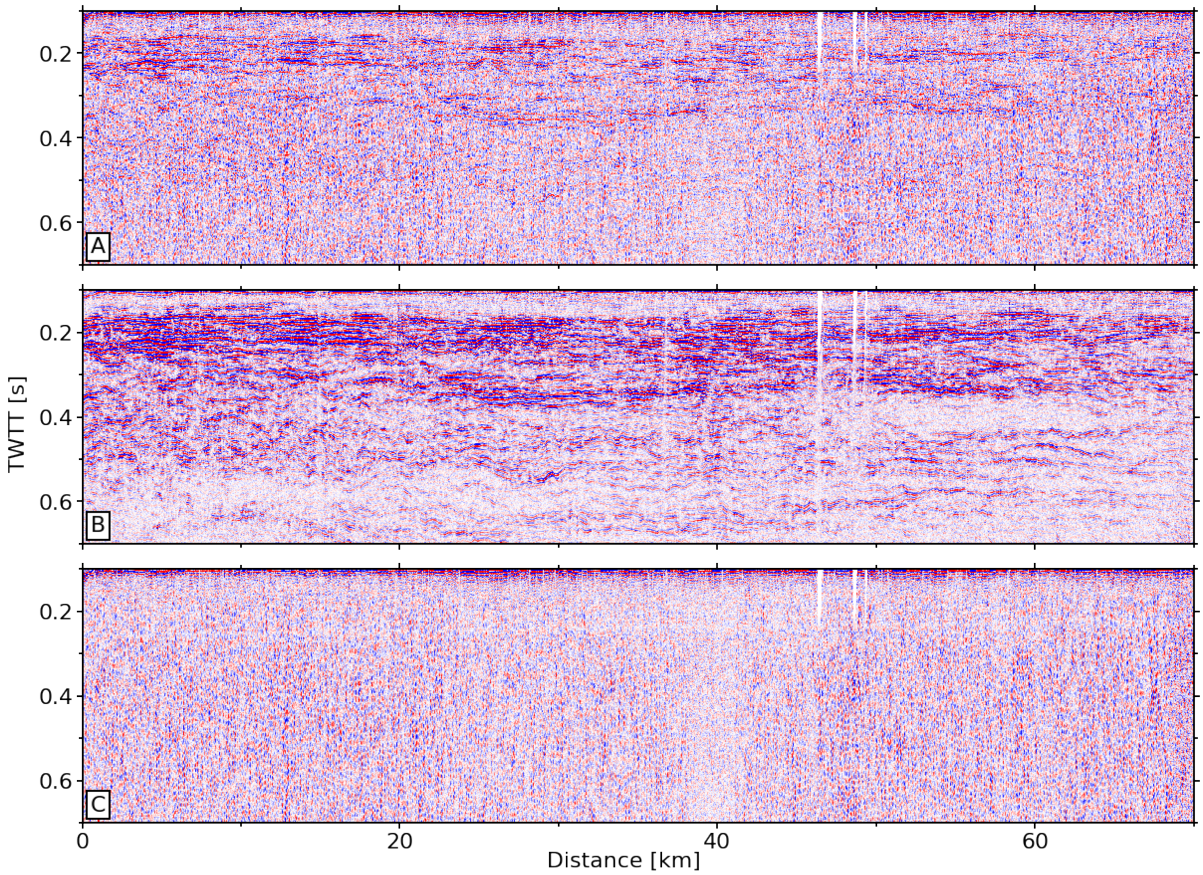

Fig. 11. Sections of seismic line 1003 of the Campeche Experiment without (A) and with (B) F-K filter applied. (C) Differences between (A) and (B) showing the removed noise.

b. Trade-off between S/N ratio and wavenumbers

Ideally, during F-K filtering, the positive wavenumber quadrant of the F-K spectrum should remain intact as it contains the entire wavenumber range needed to estimate turbulence. Although our proposed F-K filter is effective in removing previous shot multiples, other sources of noise that cannot be separated in the F-K domain such as strong ambient noise and diffractions can persist and distort the slope spectra. Under these circumstances, we have the choice to apply a fan-shape F-K filter to further remove high-wavenumber noise by sacrificing a portion of high wavenumbers in the positive wavenumber quadrant, thereby improving the S/N ratio (Fig. 10G). To illustrate its effectiveness, we applied this method to the noise-free synthetic, CREST, and Campeche seismic data (Fig. 12).

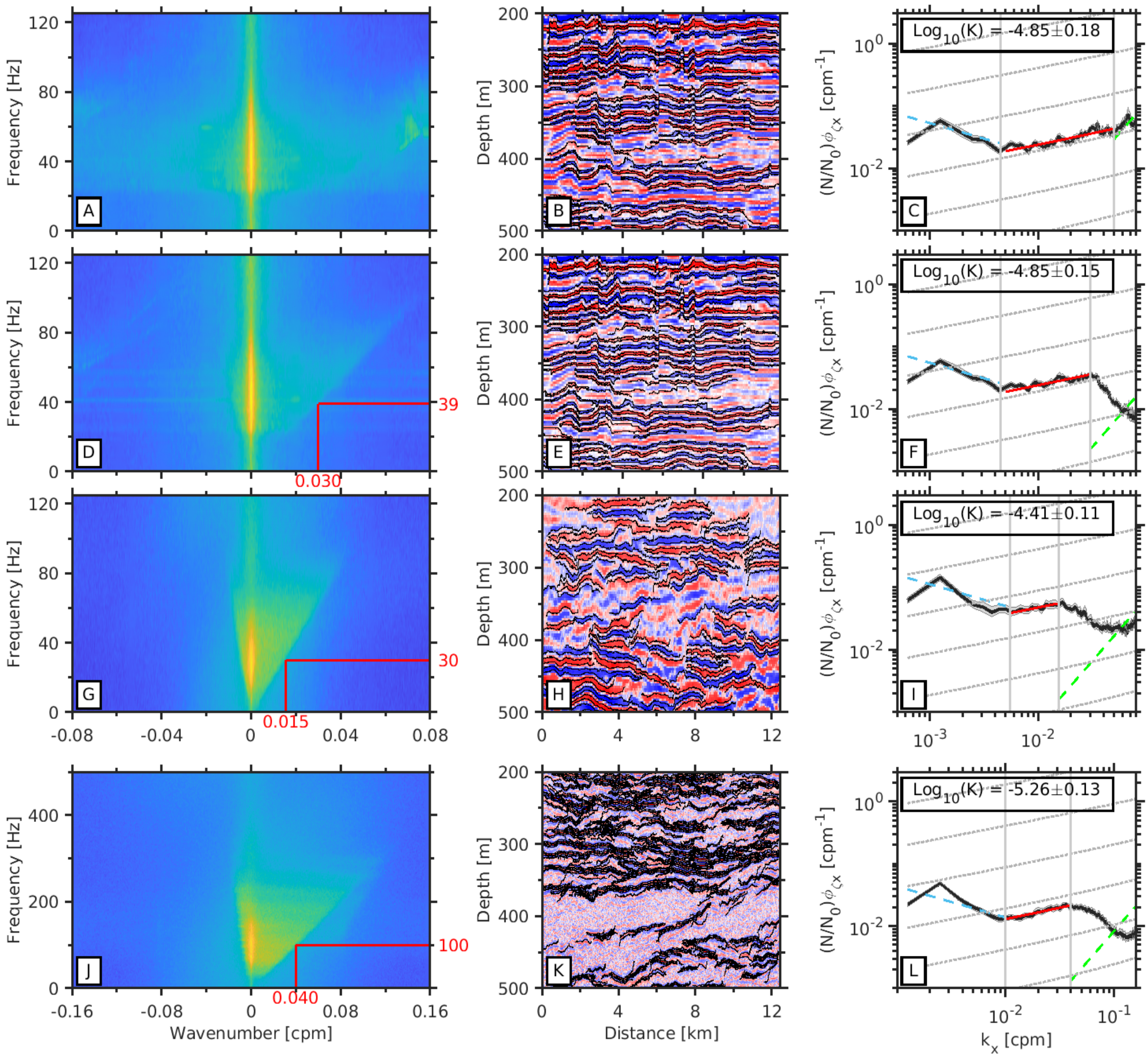

Fig. 12. The relationships between F-K filters and roll-off wavenumbers in slope spectra. (A) F-K spectrum of the synthetic seismic section in (B). (C) Average slope spectrum calculated from tracked reflections in (B). (D-F) Same for F-K filtered synthetic seismic section (F-K filter: -1, 4.8 ms/trace). Red annotations in (D) showing the correspondence between the central frequency of data in (B, E) and the roll-off wavenumber in (F) along the edge of the F-K filter in the positive wavenumber quadrant. (G-I) Same for the CREST data (F-K filter: -1, 3.5 ms/trace). (J-L) Same for the Campeche data (F-K filter: -0.5, 1.25 ms/trace). Note the change of axes in (J-L) due to different frequency bandwidth and CMP spacing of the Campeche Experiment. Also note the significant increase of resolution in (K) compared to (B),

(E), and (H). Color scheme for slope spectra is the same as in Fig. 4. Uncertainties of diffusivities only account for errors in buoyancy frequency and straight-line fitting.

First, applying a fan-shape F-K filter on the synthetic section (Fig. 12A, 12D) demonstrates the superiority of this method over a smoothing filter as it maintains the correct energy level of the spectrum, ensuring that the derived turbulent diffusivity remains unchanged (comparing diffusivities in Fig. 12C and 12F). Although this trade-off method also induces a spectrum roll-off in the reflection slope spectrum (Fig. 12F), the remaining turbulence subrange is still long enough to estimate turbulence with high fitting accuracy because LAST extends to relatively low wavenumbers. Furthermore, since the F-K filter was applied on NMO-corrected shot gathers, the form of the retained F-K spectrum naturally transfers to the post-stack data which also underwent NMO correction before stacking. This characteristic offers the flexibility to control the roll-off wavenumber of the turbulence subrange based on the dominant frequency of the post-stack data. Take the synthetic section as an example, the roll-off wavenumber (0.03 cpm) in the reflection slope spectrum (Fig. 12F) is related to the central frequency (39 Hz) of the seismic data (Fig. 13A) along the slope of the F-K filter in the positive wavenumber quadrant (Fig. 12D). Critically, this relationship holds true for field seismic data (Figs. 12, 13). The following equations show how the slopes of the F-K filter can be derived from the central frequency of the data and a user-defined roll-off wavenumber, for both the synthetic experiment and Campeche data, which have 6.25 m and 3.125 m receiver spacing, respectively:

Synthetic:

$$\frac{k_r}{f_c} = \frac{0.03\ cycles/m}{39\ cycles/s} = \frac{0.03 \times 6.25/trace}{39/1000\ ms} = \frac{0.1875/trace}{0.039/ms} = 4.8\ ms/trace \tag{6}$$

Campeche:

$$\frac{k_r}{f_c} = \frac{0.04\ cycles/m}{100\ cycles/s} = \frac{0.04 \times 3.125/trace}{100/1000\ ms} = \frac{0.125/trace}{0.1/ms} = 1.25\ ms/trace \tag{7}$$

where k_r represents roll-off wavenumber, f_c is the central frequency of the data. In this way, we can quantitatively determine the length of the retained turbulence subrange.

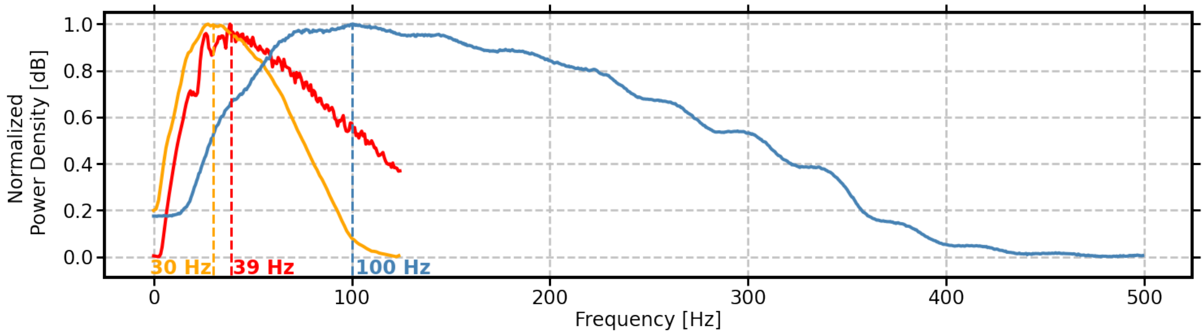

Fig. 13. Frequency spectra of the synthetic (red), the CREST (orange), and the Campeche (blue) seismic sections shown in Fig. 12. Annotations mark the central frequencies of each dataset.

The importance of this quantitative analysis stems from the intermittence and heterogeneity of turbulent mixing in the ocean (Waterhouse et al., 2014). From the perspective of downscale energy cascade, the crossover wavenumber between the internal wave and turbulence subrange is linked to the level of internal wave energy, thereby influencing the intensity of turbulence (section 2.1). This characteristic results in varying crossover wavenumbers, or, in other words, varying lengths of turbulence subranges across a seismic transect, which means a uniform smoothing across the entire seismic section might lead to excessive removal of turbulence subranges in more calmer locations where turbulence subranges start at higher wavenumbers. With the proposed F-K filter, we can iteratively adjust the filter design for different segments along a seismic transect, ensuring the fidelity of turbulence subrange and achieving a better S/N ratio.

In summary, the fan-shape F-K filter offers three advantages: (1) preserves the correct energy level of reflection slope spectra, (2) further improves S/N ratio of the seismic data, (3) provides quantitative control over the different S/N ratios and varying lengths of turbulence subranges along a seismic transect.

6. Discussion

a. Comparison with microstructure measurements

Since the discovery and development of seismic slope spectra method, seismic-derived mixing rates have not been carefully benchmarked against direct measurement of turbulence, which has stunted the prosperity of seismic oceanography. This gap is attributed not only to the absence of a standardized data processing approach, but also to the scarcity of existing microstructure measurements. Here, two of our sets of seismic data, the CREST and Hawaii experiments, are positioned in geological settings resembling those of two landmark oceanographic observations that unveiled the critical sinks of energy dissipation in the ocean: the BBTRE and HOME (Polzin et al., 1997; Rudnick et al., 2003). The environments where BBTRE and HOME took place encompass a broad range of turbulence levels, ranging from the energetic ridges to the quiescent ocean interior. Seismic data are processed using the technique described above and reach an average S/N ratio higher than 9 using the criterion by Holbrook et al. (2013). We compare the two kinds of measurements by taking depth averages within bins along spatial directions perpendicular to the mean axes of the bathymetric objects. Although the comparison is not coincident, our work provides valuable information in three aspects: (1) examine the fidelity of seismic-derived diffusivities under different environments, (2) extend observational records temporally and geographically, (3) provide insights into quantitative parametrization of turbulent mixing for numerical models.

1) HAWAIIAN RIDGE (HOME)

HOME was designed to examine the energy budget of an important open-ocean site of internal tide generation using several observational components ((Rudnick et al., 2003; Klymak et al., 2006). One of the components was conducted by the towed instrument Marlin in the Kauai Channel on a cross-ridge track at depths of 700 and 900 m. Two seismic lines from the Hawaii Experiment are in close vicinity to this Marlin track (Fig. 5). Line06 is nearly aligned with the Marlin track but has a slight northward rotation, while Line02 is positioned southeast of the Marlin track and has a rotation towards the south. The total length of Line02 is ~533 km; however, we only utilize the central 200 km that crosses the ridge because studies discovered large isopycnal displacements within about 100 km of the ridge in the Kauai Channel (Rudnick et al., 2003). Additionally, Hurricane Olivia occurred 10 days before the seismic data acquisition (Cangialosi and Jelsema, 2019). Focusing on areas adjacent to the ridge can help minimize the influence of factors other than topography, such as the dissipation of near-inertial energy, which could contribute to enhanced mixing (Fer, 2014). For both measurements, we follow Klymak et al. (2006) to take averages of diffusivities in 5-km-wide data bins between depths of 700 to 900 m, and the spatial coordinates of the bins are defined relative to the mean ridge direction, with positive distance in the northeast direction (Fig. 14). Average diffusivities from seismic data are calculated using diffusivities derived from each individual reflections within bins. Reflections longer than 0.8 km are used for spectra analysis (Krahmann et al., 2009). This comparison is more compelling than previous seismic-hydrographic comparisons for two reasons: (1) they are both horizontally continuous measurements, (2) they both represent “snapshots” of ocean states, no systematic bias due to different temporal scales are introduced during averaging (Whalen, 2021).

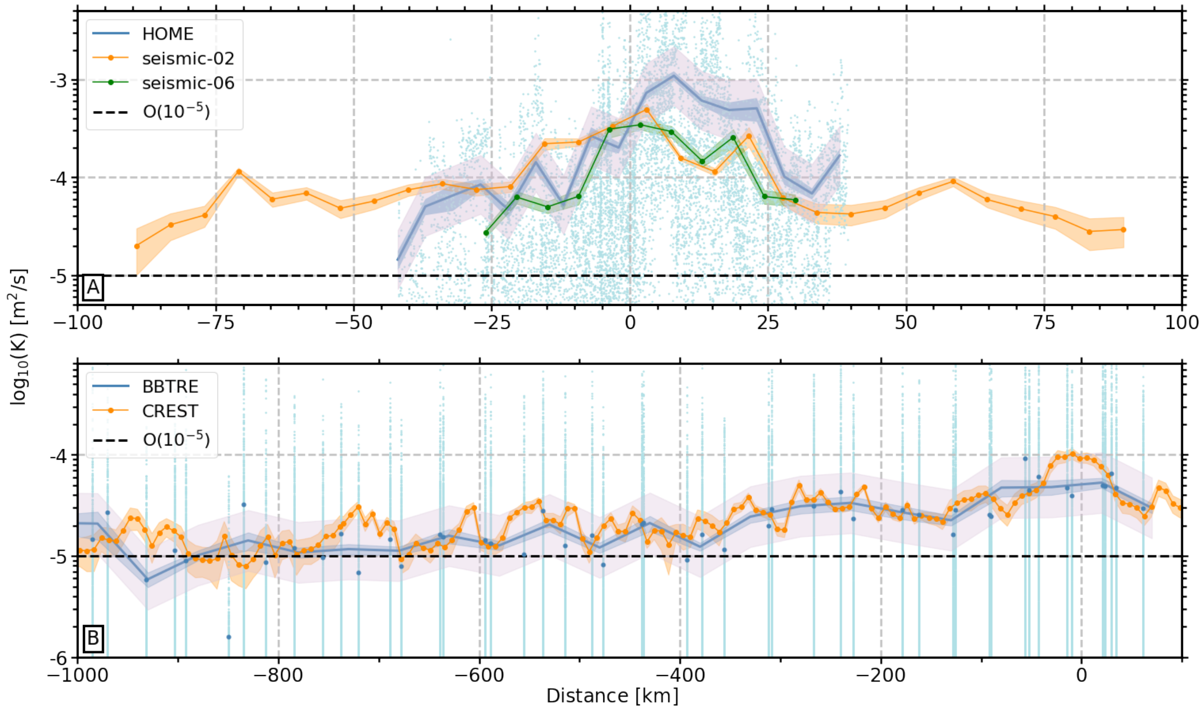

Fig. 14. Comparison between seismic and microstructure measurements as a function of distance. (A) Diffusivities in cross-ridge direction for the Kauai Channel. (B) Diffusivities away from the Mid-Atlantic Ridge. Blue, orange, green shades represent 95% confidence intervals. Pink shades bounds the ± 0.3 logarithmic units of microstructure measured diffusivities. Blue dots = average diffusivities of each BBTRE vertical profile. Light blue dots = microstructure samples. Dashed black lines = background diffusivity of 10^{-4} m^2 s^{-1}.

Similar to the microstructure measurements, the diffusivities derived from seismic data exhibit highest values over the ridge crest and extend across the width of the ridge saddles (Fig. 14A). The highest mean diffusivities for Line06 and Line02 are 3.4×10^{-4} m^2/s, and 4.9×10^{-4} m^2/s, respectively, an order of magnitude higher than the background level of 10^{-5} m^2/s. Notably, the diffusivities measured by Line06 and Marlin exhibit similarity: (1) rapid decay to the background level within 40-60 km from the ridge, (2) comparable widths of enhanced diffusivities over the ridge top spanning approximately 20-30 kilometers, and (3) significant drop-off from ~2×10^{-4} m^2/s to ~6×10^{-5} m^2/s occurring around -7.5 km (Fig. 14A). However, for Line02, the decay is much slower, taking ~100 km for diffusivities to decrease to 10^{-5} m^2/s. The coherence between Line06 and Marlin and their differences from Line02 suggest a pattern change of energy dissipation. The corrugated bathymetry beneath Line02 on both sides of the ridge favors the generation of high-mode internal tides so that more energy is dissipated locally (Vic et al., 2019), contributing to the longer decay distance. In contrast, along Line06 and Marlin track where steep topographic relief is present, more energy propagates away as low-mode internal tides (Rudnick et al., 2003; Klymak et al., 2006). The observed two patterns support the importance of topography in distributing internal wave energy in the ocean, as previous studies have shown the different forms of tidal energy transfer affected by the ratios between the tidal beam and topographic slopes (Klymak et al., 2011). Bottom scattering of low-mode internal waves into high-modes that facilitate mixing might also contribute to the observed differences (Müller and Xu, 1992; Bühler and Holmes-Cerfon, 2011).

It is noteworthy that neither Line06 nor Line02 capture the extremely high diffusivities measured by microstructure data (e.g., 10^{-3} m^2/s), due to the limitation of the reflection slope spectra method, which depends on tracking continuous reflections. Krahmann et al. (2009) suggest that reflections with wavelengths between 0.8 and 2.8 km can be approximated as isopycnals so that the assumption of the slope spectra holds true. We conducted tests by using reflection lengths of 0.8 km and 1.6 km and found that in areas away from the ridge where background values are found, both cases yield similar levels of diffusivities. However, close to the ridge where turbulence is high, using longer reflections severely underestimates diffusivities because only stronger reflections are tracked and spectrally analyzed. These results are expected as high amplitude, continuous reflections denote relatively stable stratification and weaker turbulence. In contrast, reflections become choppier as turbulence intensifies, reducing the efficacy of the tracking algorithm (Holbrook et al., 2013; Fortin et al., 2016). Our experiment suggests that it is preferable to use shorter reflections for spectra analysis in energetic regions to capture the enhanced turbulence. The choice of reflection length clearly influences how well turbulence is represented by slope spectra, an issue that remains unresolved and as such more quantitative analysis is needed in the future. Ideally, with technical advancement, spectra could be computed directly from seismic-inverted sections of temperature and salinity, avoiding the need to track reflections (Dickinson and Gunn, 2022).

For the Hawaiian experiment, the average uncertainty of spectra fitting for both lines is up to 0.25 in logarithmic units. In the selected depth range of 700-900 m, the average uncertainty of N is less than 4% (Fig. 6), it will introduce an uncertainty of 0.018 in logarithmic units. Combined with the uncertainties from other parameters summarized in section 2.1 and assuming independence in error propagation, the total uncertainty for $\log_{10}(K_\rho)$ is ~0.33. Compare with microstructure measurements, seismically derived diffusivities are generally within ± 0.3 logarithmic units off the ridge crest (Fig. 14A).

2) MID-ATLANTIC RIDGE (BBTRE)

BBTRE is one of the pioneering physical oceanographic observations that examine the intensity, spatial distribution, and mechanisms of mixing across the entire water column over a large region (Polzin et al., 1997). Here, we use the High-Resolution Profilers (HRP) microstructure data collected during the second leg of the BBTRE in 1997 between 21°-23° S. These stations were relatively densely spaced and sampled along the east-west direction, spanning from the top of the Mid-Atlantic Ridge to the smooth topography of ocean interior (Fig. 5).

The CREST seismic survey is positioned in a similar environment along 30° S, providing an opportunity, for the first time, to compare seismic-derived diffusivities with microstructure measurements over a significant distance. We only selected data between 200-1000 m in the upper ocean as the seismic data are noisier in the deeper regions, resulting in fewer trackable reflections. Including data below 1000 m will bias the comparison due to inconsistent sampling density and data quality (Fig. 4A). Following the strategy in section 5.1.1, we take depth-averages within bins as a function of distance away from the Mid-Atlantic Ridge for both measurements (Fig. 14B). Since the HRPs are not evenly spaced, we average data within 50-km bins to reduce spatial bias, whereas seismic data is averaged in 5-km bins to take advantage of its high spatial resolution. Our tests on different bin sizes suggest lesser impact on results, indicating that spatial bias stemming from the choice of bins is not significant.

In comparison to the results around the Hawaiian Ridge in the last section (6.1.1), CREST and BBTRE show better agreement on the level of mixing rates. For both measurements, diffusivities are close to 10^{-4} m^2/s over the top of the ridge and decrease gently over a significant distance to the background level more than 800 km away from the ridge (Fig. 14B). Notably, the decay patterns of K_ρ with respect to the distances from the crest of ridges, x, can be approximated by similar 1/2 power-law relationships (Fig. 15). Following Tang (2021, 2022), we have:

$$\log_{10} K_\rho^{MC}(x) = -0.0241 x^{1/2} - 4.1642 \quad (8)$$

$$\log_{10}K_{\rho}^{MB}(x) = -0.0251x^{1/2} - 4.1910 \tag{9}$$

where $K_\rho^{MC}(x)$ and $K_\rho^{MB}(x)$ are the model diffusivity for CREST and BBTRE, respectively. The mean fitting residual $\langle|\Delta\log_{10}K_\rho^{M}(x)|\rangle = \langle|\log_{10}K_\rho(x) - \log_{10}K_\rho^{M}(x)|\rangle$ is 0.116 for CREST and 0.112 for BBTRE in logarithmic units (Fig. 15). The two empirical relationships suggest that along zonal direction at two different latitudes in the South Atlantic, the nonlinear decay of turbulence follows a relatively consistent pattern from the Mid-Atlantic Ridge into the ocean basin.

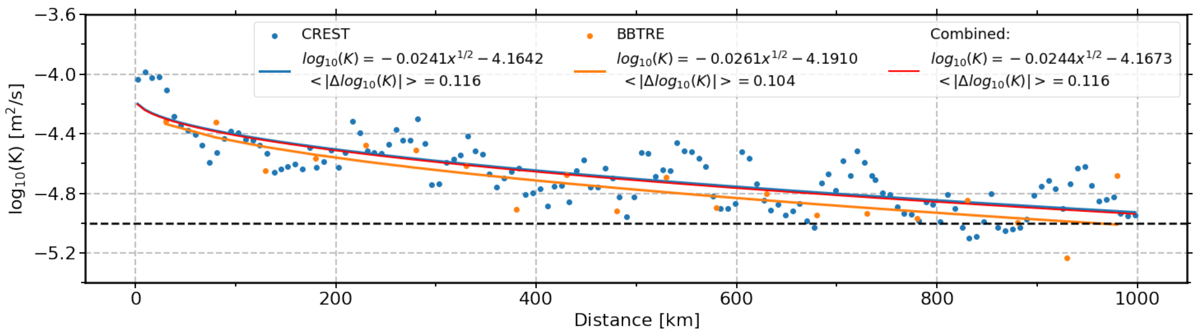

Fig. 15. Power-law fittings of average diffusivities in Fig. 14B for CREST (blue), BBTRE (orange), and the two combined (red), showing decay of mixing away from Mid-Atlantic Ridges up to 1000 km. $\langle|\Delta\log_{10}K|\rangle$ is the mean fitting residual. Dashed black lines = background diffusivity of 10^{-4} m^2 s^{-1}.

Within 1000 km from mid-ocean ridges, the mechanisms contributing to energy dissipation are complex. For instance, breaking and dissipation of high-mode internal tides (St. Laurent and Garrett, 2002; Vic et al., 2019), scattering of low-mode internal tides off irregular topography (de Lavergne et al., 2019), different types of wave-wave interactions, and lee waves can all play a role (Whalen et al., 2020). Therefore, the consistency observed in the upper ocean at two different locations is surprising. It could be related to changes in the roughness of the seafloor (Polzin et al., 1997; Waterhouse et al., 2014). Or it might simply be due to increasing water depths away from the ridge, resulting in decreased disturbance in the upper ocean from breaking of high-mode internal tides. It is also possible that some form of resonance exists geographically between different mechanisms of energy dissipation which might provide insights into parametrization. While it is impossible for us to discern between mechanisms, our results support the notion of a high tidal energy conversion rate by abyssal hills (Vic et al., 2019). Given that it took almost 1000 km for diffusivity to decay to the background level, and mode 1 internal tide is unique in its long-range propagation (>1000 km) (Alford and Zhao, 2007; Zhao et al., 2016), internal tides with modes > 1 likely dissipated within 1000 km from the Mid-Atlantic Ridge. From the perspective of wave-wave interaction, BBTRE measured turbulence is more likely to be higher than CREST due to a process known as parametric subharmonic instability occurring equatorward of 29°, when high-mode internal waves interact with a low-mode wave with twice their frequency (Hibiya and Nagasawa, 2004; MacKinnon et al., 2013). However, our results show the opposite; CREST measured diffusivities are slightly higher than BBTRE. This discrepancy might be attributed to the residual noise in the seismic data that overestimates the spectra energy (section 4.2). However, it could also be caused by a storm event happened ~30 days prior to the seismic survey, which generated near-inertial waves and contributed to elevated turbulence in the upper ocean (Wei et al., 2022).

For the CREST experiment, the average uncertainty of spectra fitting for both lines is up to 0.16 in logarithmic units. In the selected depth range of 200-1000 m, the average uncertainty of N is less than 5% (Fig. 6); it will introduce an uncertainty of 0.021 in logarithmic units. The combined total uncertainty for $\log_{10}(K_\rho)$ is ~0.27. Compare with microstructure measurements, seismic-derived diffusivities are within ± 0.3 logarithmic units over the analyzed distance of 1000 km (Fig. 14B).

b. Toward a standardized workflow

Through the comparison with microstructure data, we have demonstrated that the seismic-derived diffusivities are in good agreement with microstructure measurements in different oceanographic environments, within margins of error. While not concurrent, the seismic-derived diffusivities are generally within ± 0.3 logarithmic units of the microstructure measurements (except for extreme values), indicating the seismic method is capable of measuring ocean turbulence with confidence. The analysis of this study underscores that the accuracy of the seismic method relies on maintaining the correct energy level of the slope spectra. The key in achieving this goal lies in preserving the true reflection amplitude during data processing while minimizing noise as much as possible. While a S/N ratio higher than 9 is recommended, an even higher S/N ratio should be considered ideal. Building upon the recommendations of Holbrook et al. (2013), we propose a standardized workflow featuring an iterative F-K filtering process suitable for legacy marine seismic dataset whose original acquisition was not devised for water column research (Fig. 16). The iterative approach allows for balancing considerations between F-K filter design, S/N ratio, and spatial heterogeneity of turbulent mixing. It is advisable to apply differentiated F-K filters to data with varying S/N ratios across a seismic section, using user-defined spatial windows. The fan width of the F-K filters can also be iteratively adjusted based on the length of the turbulence subrange in the resulting slope spectra.

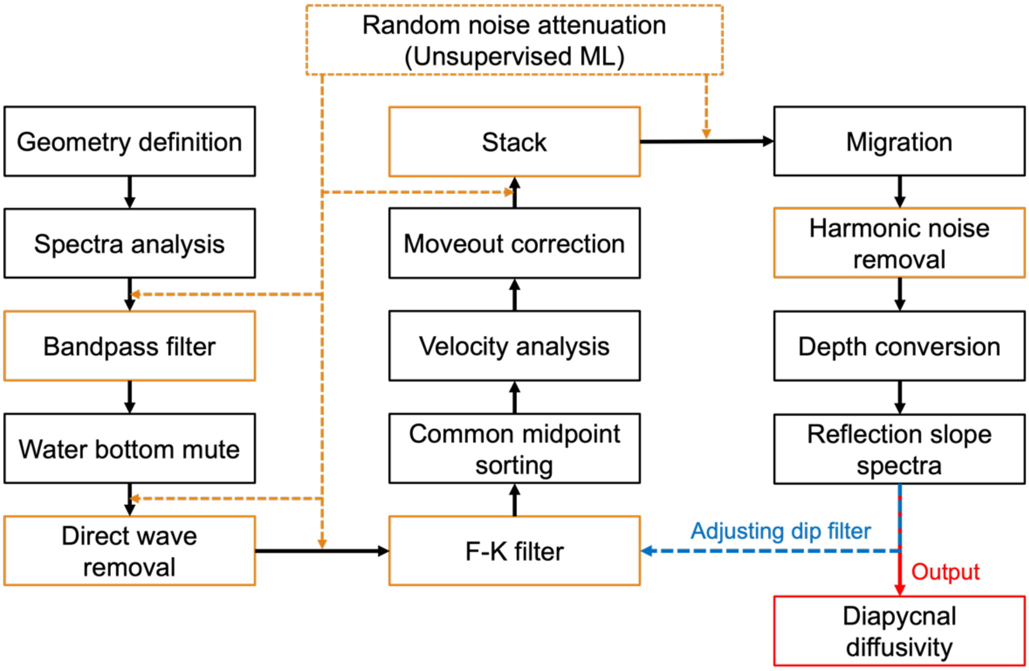

Fig. 16. A standardized workflow for using legacy seismic data to calculate diapycnal diffusivity. Orange boxes denote steps related to noise attenuation. Dashed orange lines pointing to the processing phase where machine learning based methods could be useful.

Nevertheless, this workflow represents an expedient approach that adopts a trade-off strategy between S/N ratio and high-wavenumber turbulence information. Moreover, the F-K filter is not efficient on data acquired by small acquisition systems with short streamers (e.g., 24 channels) as they do not provide enough moveout differences between reflections and coherent noise. Future endeavors might explore advanced techniques such as machine learning (ML) based method to keep the slope spectra intact. Attempts have been made using a supervised denoising convolutional neural network (DnCNN) on post-stack sparker data (Zhang et al., 2017; Jun et al., 2020). However, DnCNN is not very effective for legacy seismic data collected by air-gun sources which generate high-amplitude reflections and coherent noise simultaneously. This is likely due to the lack of ground truth to build high quality training set. Therefore, future work employing unsupervised ML on either pre-stack or post-stack data would be valuable to improve the workflow. Because stacking is essential in producing images of thermohaline fine structures, ML denoising on pre-stack data might be challenging due to weaker reflection amplitudes, which could potentially be misinterpreted as noise by ML algorithms. In any case, with proper tools to ensure the spectra integrity, seismic oceanography can provide a global inventory of oceanic horizontal-wavenumber spectra which could greatly improve our understanding of energy cascade across different length scales and thereby building better parametrizations for climate models (Dickinson and Gunn, 2022).

7. Conclusions

In this study, we discussed the challenges of using legacy marine seismic reflection data to faithfully derive turbulent diapycnal diffusivities. Through full-wavefield synthetic modeling, we have shown that the energy level of reflection slope spectra is sensitive to the S/N ratio of the seismic data, such that increasing noise levels lead to increasing overestimation of diffusivities. In addition, the turbulent subranges of the slope spectra are easily affected by changes in reflection amplitudes which delineate the vertical displacements of isopycnals. Our results emphasize the necessity of a seismic data processing strategy that preserve true reflection amplitudes while minimizing noise simultaneously.

To tackle these problems, we developed a workflow that adopts an iterative spectrum filtering approach which allows for quantitative balancing between the considerations of filter design, S/N ratio, and spatial heterogeneity of turbulent mixing. The workflow also leaves spaces for future integration of machine learning techniques to further enhance S/N ratios. Its successful implementation on three seismic datasets collected by different acquisition systems proves its reliability and versatility. The resulted diapycnal diffusivities agree well with the direct measurements of turbulence collected in the Brazil Basin and at the Hawaiian Ridge, with diffusivities within ± 0.3 logarithmic units of the microstructure measurements when diffusivities are weaker than $\sim 10^{-3}$ m^2/s. The comparison also highlights the recommendation of using seismic data with S/N ratios higher than 9 in future applications.

Combining observations from the microstructure and seismic data underscores the critical role of topography in transferring energy across lengths scales through the internal wave continuum. While discerning individual contributing factors remains challenging, our results across the Kauai Channel and away from the Mid-Atlantic Ridge both support the phenomenon that small scale topography facilitates the cascade of energy from larger to smaller scales and ultimately to turbulence, contributing to extended decay distance of mixing. The surprising consistency between the decay of mixing at different latitudes in the South Atlantic implies internal tides with modes greater than 1 are likely all dissipated within 1000 km of mid-ocean ridges. The constructed empirical models of diffusivity as a function of distance might provide insights on climate model parametrizations. However, more observations and theory development are required to fully understand the evolution of mixing across ocean basins.

Building upon the recommendations of Holbrook et al. (2013), our proposed workflow is a key advance towards standardization of seismic derived mixing rates. However, more efforts are needed in the future. For example, we briefly discussed how the choice of tracked reflection lengths affects the derived diffusivities in high turbulence environment, emphasizing the need to examine the validity of the assumption that reflections approximate isopycnals under different turbulence levels. Studies looking into the length scales of shear instabilities relative to the seismic source wavelength are also desirable. Once seismic methods for estimating mixing are standardized, existing seismic datasets will provide a way to investigate possible changes in oceanic mixing during the previous four decades, when few other measurements were available (Dickinson and Gunn, 2022). Furthermore, although our proposed workflow is tailored to standardizing the processing of legacy seismic, it provides valuable insights into future dedicated seismic oceanography surveys, where portable acquisition systems are expected (Ruddick, 2018). More considerations are required in planning shot spacing and recording length to prevent interference from previous shot multiples and to achieve better S/N ratios.

Acknowledgments.

We are grateful to the captains, crews, and science parties of cruises MGL1601, MGL1806 of the R/V *Marcus G. Langseth* and JS2203 of the *R/V Justo Sierra* for their acquisition of high-quality seismic data. We acknowledge NSF-OCE-1928888, CONTEX 2018-38A, and a Pre-Drilling Activity Award from the U.S. Science Support Program (NSF prime award OCE - 1450528) to Lowery, which funded acquisition and processing of the Campeche Bank data. We are grateful to Dr. Ilker Fer for providing instructions on constructing the synthetic turbulence model. We thank Dr. Amy Waterhouse for compiling the microstructure database and Dr. Jody Klymak for sharing the HOME dataset. We also thank Dr. Robert Reece and Dr. Justin Estep for their support during the beginning stage of this work. We are also grateful to UTIG for providing necessary computing resources. Seismic data processing was carried out using Seismic Unix (https://github.com/JohnWStockwellJr/SeisUnix) and the Paradigm seismic software application, Echos, provided by AspenTech. GO-SHIP observations were

downloaded from CLIVAR and Carbon Hydrographic Data Office (https://cchdo.ucsd.edu/) for expocodes A10 33RO20110926. Microstructure data were downloaded and processed using the software by the oceanographic mixing community (https://github.com/OceanMixingCommunity). CTDs around Hawaii was obtained via the Hawaii Ocean Time-series HOT-DOGS application; University of Hawai'i at Mānoa; National Science Foundation Award # 1756517. CTD data were analyzed using GSW TEOS-10 equation of state for seawater (github.com/TEOS-10/GSW-Python).

Data Availability Statement.

Seismic data is available from the Marine Geoscience Data System's Academic Seismic Portal. MGL1601 DOI: 10.1594/IEDA/323597; MGL1806 DOI: 10.1594/IEDA/324706; JS2203 DOI: 10.26022/IEDA/331509.

REFERENCES

Alford, M., & Munk, W. (2019). Internal Tidal Mixing.

Alford, M. H. (2003). Redistribution of energy available for ocean mixing by long-range propagation of internal waves. *Nature, 423*(6936), 159-162.

Alford, M. H., & Zhao, Z. (2007). Global patterns of low-mode internal-wave propagation. Part I: Energy and energy flux. *Journal of Physical Oceanography, 37*(7), 1829-1848.

Batchelor, G., Howells, I., & Townsend, A. (1959). Small-scale variation of convected quantities like temperature in turbulent fluid Part 2. The case of large conductivity. *Journal of Fluid Mechanics, 5*(1), 134-139.

Bell Jr, T. (1975). Topographically generated internal waves in the open ocean. *Journal of Geophysical Research, 80*(3), 320-327.

Bray, N. A., & Fofonoff, N. (1981). Available potential energy for MODE eddies. *Journal of Physical Oceanography, 11*(1), 30-47.

Bühler, O., & Holmes-Cerfon, M. (2011). Decay of an internal tide due to random topography in the ocean. *Journal of Fluid Mechanics, 678*, 271-293.

Cangialosi, J., & Jelsema, J. (2019). National Hurricane Center/Central Pacific Hurricane Center Tropical Cyclone Report—Hurricane Olivia (EP172018). 2019. In.

Carbotte, S. M., Arnulf, A., Spiegelman, M., Lee, M., Harding, A., Kent, G., . . . Nedimović, M. (2020). Stacked sills forming a deep melt-mush feeder conduit beneath Axial Seamount. *Geology, 48*(7), 693-697.

Caulfield, C. (2021). Layering, instabilities, and mixing in turbulent stratified flows. *Annual Review of Fluid Mechanics, 53*, 113-145.

CCHDO. (2023). CCHDO Hydrographic Data Archive. *UC San Diego Library Digital Collections*. doi:https://doi.org/10.6075/J0CCHAM8

Corrsin, S. (1951). On the spectrum of isotropic temperature fluctuations in an isotropic turbulence. *Journal of Applied Physics, 22*(4), 469-473.

D'Asaro, E. A. (1985). The energy flux from the wind to near-inertial motions in the surface mixed layer. *Journal of Physical Oceanography, 15*(8), 1043-1059.

de Lavergne, C., Falahat, S., Madec, G., Roquet, F., Nycander, J., & Vic, C. (2019). Toward global maps of internal tide energy sinks. *Ocean Modelling, 137*, 52-75.

Dickinson, A., & Gunn, K. (2022). The Next Decade of Seismic Oceanography: Possibilities, Challenges and Solutions. Front. *Mar. Sci, 9*, 736693.

Dickinson, A., White, N., & Caulfield, C. (2017). Spatial variation of diapycnal diffusivity estimated from seismic imaging of internal wave field, Gulf of Mexico. *Journal of Geophysical Research: Oceans, 122*(12), 9827-9854.

Dickinson, A., White, N., & Caulfield, C. (2020). Time‐Lapse Acoustic Imaging of Mesoscale and Fine‐Scale Variability within the Faroe‐Shetland Channel. *Journal of Geophysical Research: Oceans, 125*(8), e2019JC015861.

Estep, J., Reece, R., Kardell, D. A., Christeson, G. L., & Carlson, R. L. (2019). Seismic Layer 2A: Evolution and Thickness From 0‐ to 70‐Ma Crust in the Slow‐Intermediate Spreading South Atlantic. *Journal of Geophysical Research: Solid Earth, 124*(8), 7633-7651.

Falder, M., White, N. J., & Caulfield, C.-c. P. (2016). Seismic imaging of rapid onset of stratified turbulence in the south Atlantic Ocean. *Journal of Physical Oceanography, 46*(4), 1023-1044.

Fer, I. (2014). Near-inertial mixing in the central Arctic Ocean. *Journal of Physical Oceanography, 44*(8), 2031-2049.

Fortin, W. F., Holbrook, W. S., & Schmitt, R. W. (2016). Mapping turbulent diffusivity associated with oceanic internal lee waves offshore Costa Rica. *Ocean Science, 12*(2), 601-612.

Fortin, W. F., Holbrook, W. S., & Schmitt, R. W. (2017). Seismic estimates of turbulent diffusivity and evidence of nonlinear internal wave forcing by geometric resonance in the South China Sea. *Journal of Geophysical Research: Oceans, 122*(10), 8063-8078.

Garrett, C., & Munk, W. (1975). Space‐time scales of internal waves: A progress report. *Journal of Geophysical Research, 80*(3), 291-297.

Gill, A. (1984). On the behavior of internal waves in the wakes of storms. *Journal of Physical Oceanography, 14*(7), 1129-1151.

Gill, A. E. (1982). *Atmosphere-ocean dynamics* (Vol. 30): Academic press.

Graves, R. W. (1996). Simulating seismic wave propagation in 3D elastic media using staggered-grid finite differences. *Bulletin of the seismological society of America, 86*(4), 1091-1106.

Gregg, M. (1989). Scaling turbulent dissipation in the thermocline. *Journal of Geophysical Research: Oceans, 94*(C7), 9686-9698.

Gulick, S. P., Barton, P. J., Christeson, G. L., Morgan, J. V., McDonald, M., Mendoza-Cervantes, K., . . . Vermeesch, P. M. (2008). Importance of pre-impact crustal structure for the asymmetry of the Chicxulub impact crater. *Nature Geoscience, 1*(2), 131-135.

Gulick, S. P. S., Reece, R., Christeson, G., Van Avendonk, H., Worthington, L., & Pavlis, T. L. (2013). Seismic images of the Transition fault and the unstable Yakutat–Pacific–North American triple junction. *Geology, 41*(5), 571-574.

Gunn, K. L., Dickinson, A., White, N., & Caulfield, C.-C. P. (2021). Vertical Mixing and Heat Fluxes Conditioned by a Seismically Imaged Oceanic Front. *Frontiers in Marine Science, 8*, 697179.

Hibiya, T., & Nagasawa, M. (2004). Latitudinal dependence of diapycnal diffusivity in the thermocline estimated using a finescale parameterization. *Geophysical Research Letters, 31*(1).

Holbrook, W. S., Fer, I., Schmitt, R. W., Lizarralde, D., Klymak, J. M., Helfrich, L. C., & Kubichek, R. (2013). Estimating oceanic turbulence dissipation from seismic images. *Journal of Atmospheric and Oceanic Technology, 30*(8), 1767-1788.

Holbrook, W. S., Páramo, P., Pearse, S., & Schmitt, R. W. (2003). Thermohaline fine structure in an oceanographic front from seismic reflection profiling. *Science, 301*(5634), 821-824.

Jun, H., Jou, H.-T., Kim, C.-H., Lee, S. H., & Kim, H.-J. (2020). Random noise attenuation of sparker seismic oceanography data with machine learning. *Ocean Science, 16*(6), 1367-1383.

Klymak, J. M., Alford, M. H., Pinkel, R., Lien, R.-C., Yang, Y. J., & Tang, T.-Y. (2011). The breaking and scattering of the internal tide on a continental slope. *Journal of Physical Oceanography, 41*(5), 926-945.

Klymak, J. M., & Moum, J. N. (2007a). Oceanic isopycnal slope spectra. Part I: Internal waves. *Journal of Physical Oceanography, 37*(5), 1215-1231.

Klymak, J. M., & Moum, J. N. (2007b). Oceanic isopycnal slope spectra. Part II: Turbulence. *Journal of Physical Oceanography, 37*(5), 1232-1245.

Klymak, J. M., Moum, J. N., Nash, J. D., Kunze, E., Girton, J. B., Carter, G. S., . . . Gregg, M. C. (2006). An estimate of tidal energy lost to turbulence at the Hawaiian Ridge. *Journal of Physical Oceanography, 36*(6), 1148-1164.

Kolmogorov, A. N. (1941). The local structure of turbulence in incompressible viscous fluid for very large Reynolds. *Numbers. In Dokl. Akad. Nauk SSSR, 30*, 301.

Krahmann, G., Papenberg, C., Brandt, P., & Vogt, M. (2009). Evaluation of seismic reflector slopes with a Yoyo ‐ CTD. *Geophysical Research Letters, 36*(24).

Kunze, E. (2017). Internal-wave-driven mixing: Global geography and budgets. *Journal of Physical Oceanography, 47*(6), 1325-1345.

Kunze, E. (2019). A unified model spectrum for anisotropic stratified and isotropic turbulence in the ocean and atmosphere. *Journal of Physical Oceanography, 49*(2), 385-407.

Ledwell, J., Montgomery, E., Polzin, K., Laurent, L. S., Schmitt, R., & Toole, J. (2000). Evidence for enhanced mixing over rough topography in the abyssal ocean. *Nature, 403*(6766), 179.

Lindborg, E. (2006). The energy cascade in a strongly stratified fluid. *Journal of Fluid Mechanics, 550*, 207-242.

Lowery, C., Perez Cruz, L., Urrutia Fucugauchi, J., Wei, J., Austin Jr, J. A., & Standring, P. (2024a). Raw high-resolution multi-channel seismic reflection (MCS) field data from the JS2203 Gulf of Mexico Campeche Bank Seismic Survey (2022). *MGDS*. doi:10.26022/IEDA/331509

Lowery, C., Perez Cruz, L., Urrutia Fucugauchi, J., Wei, J., Austin Jr, J. A., & Standring, P. (2024b). Seismic stratigraphy of contourite drift deposits associated with the Loop Current on the eastern Campeche Bank, Gulf of Mexico. *Paleoceanography and Paleoclimatology, 39*(3), e2023PA004701.

Lueck, R. G., Wolk, F., & Yamazaki, H. (2002). Oceanic velocity microstructure measurements in the 20th century. *Journal of Oceanography, 58*, 153-174.

MacKinnon, J., Alford, M. H., Sun, O., Pinkel, R., Zhao, Z., & Klymak, J. (2013). Parametric subharmonic instability of the internal tide at 29 N. *Journal of Physical Oceanography, 43*(1), 17-28.

MacKinnon, J. A., Zhao, Z., Whalen, C. B., Waterhouse, A. F., Trossman, D. S., Sun, O. M., . . . Pinkel, R. (2017). Climate process team on internal wave–driven ocean mixing. *Bulletin of the American Meteorological Society, 98*(11), 2429-2454.

Melet, A., Legg, S., & Hallberg, R. (2016). Climatic impacts of parameterized local and remote tidal mixing. *Journal of Climate, 29*(10), 3473-3500.

Moum, J., Caldwell, D., Nash, J., & Gunderson, G. (2002). Observations of boundary mixing over the continental slope. *Journal of Physical Oceanography, 32*(7), 2113-2130.

Müller, P., & Xu, N. (1992). Scattering of oceanic internal gravity waves off random bottom topography. *Journal of Physical Oceanography, 22*(5), 474-488.

Munk, W., & Wunsch, C. (1998). Abyssal recipes II: Energetics of tidal and wind mixing. *Deep Sea Research Part I: Oceanographic Research Papers, 45*(12), 1977-2010.

Osborn, T. (1980). Estimates of the local rate of vertical diffusion from dissipation measurements. *Journal of Physical Oceanography, 10*(1), 83-89.

Osborn, T. R., & Cox, C. S. (1972). Oceanic fine structure. *Geophysical Fluid Dynamics, 3*(4), 321-345.

Palmer, M. R., Stephenson, G. R., Inall, M. E., Balfour, C., Düsterhus, A., & Green, J. (2015). Turbulence and mixing by internal waves in the Celtic Sea determined from ocean glider microstructure measurements. *Journal of Marine Systems, 144*, 57-69.

Peterson, A. K., & Fer, I. (2014). Dissipation measurements using temperature microstructure from an underwater glider. *Methods in Oceanography, 10*, 44-69.

Polzin, K., Toole, J., Ledwell, J., & Schmitt, R. (1997). Spatial variability of turbulent mixing in the abyssal ocean. *Science, 276*(5309), 93-96.

Polzin, K. L., Garabato, A. C. N., Huussen, T. N., Sloyan, B. M., & Waterman, S. (2014). Finescale parameterizations of turbulent dissipation. *Journal of Geophysical Research: Oceans, 119*(2), 1383-1419.

Rainville, L., Gobat, J., Lee, C., & Shilling, G. (2017). Multi-month dissipation estimates using microstructure from autonomous underwater gliders. *Oceanography, 30*(2), 49-50.

Reece, R., & Christeson, G. (2017). Multi-Channel Seismic Shot Data from the South Atlantic Ocean acquired during R/V Marcus G. Langseth expedition MGL1601 (2016). *MGDS*. doi:10.1594/IEDA/323597

Riley, J. J., & Lindborg, E. (2008). Stratified turbulence: A possible interpretation of some geophysical turbulence measurements. *Journal of the Atmospheric Sciences, 65*(7), 2416-2424.

Roemmich, D., Alford, M. H., Claustre, H., Johnson, K., King, B., Moum, J., . . . Purkey, S. (2019). On the future of Argo: A global, full-depth, multi-disciplinary array. *Frontiers in Marine Science, 6*, 439.

Ruddick, B. (2018). Seismic Oceanography's Failure to Flourish: A Possible Solution. *Journal of Geophysical Research: Oceans, 123*(1), 4-7.

Ruddick, B., SoNg, H., Dong, C., & Pinheiro, L. (2009). Water column seismic images as maps of temperature gradient. *Oceanography, 22*(1), 192-205.

Rudnick, D. L., Boyd, T. J., Brainard, R. E., Carter, G. S., Egbert, G. D., Gregg, M. C., . . . Lee, C. M. (2003). From tides to mixing along the Hawaiian Ridge. *Science, 301*(5631), 355-357.

Ryan, W. B., Carbotte, S. M., Coplan, J. O., O'Hara, S., Melkonian, A., Arko, R., . . . Nitsche, F. (2009). Global multi‐resolution topography synthesis. *Geochemistry, Geophysics, Geosystems, 10*(3).

Sallares, V., Mojica, J. F., Biescas, B., Klaeschen, D., & Gràcia, E. (2016). Characterization of the submesoscale energy cascade in the Alboran Sea thermocline from spectral analysis of high‐resolution MCS data. *Geophysical Research Letters, 43*(12), 6461-6468.

Schmit, R. W., Toole, J. M., Koehler, R. L., Mellinger, E. C., & Doherty, K. W. (1988). The development of a fine-and microstructure profiler. *Journal of Atmospheric and Oceanic Technology, 5*(4), 484-500.

Serov, P., Vadakkepuliyambatta, S., Mienert, J., Patton, H., Portnov, A., Silyakova, A., . . . Andreassen, K. (2017). Postglacial response of Arctic Ocean gas hydrates to climatic amelioration. *Proceedings of the National Academy of Sciences, 114*(24), 6215-6220.

Sheen, K., White, N., & Hobbs, R. (2009). Estimating mixing rates from seismic images of oceanic structure. *Geophysical Research Letters, 36*(24).

Sheen, K. L., White, N., Caulfield, C. P., & Hobbs, R. W. (2011). Estimating geostrophic shear from seismic images of oceanic structure. *Journal of Atmospheric and Oceanic Technology, 28*(9), 1149-1154.

Shillington, D., Watts, A., Dunn, R., Wessel, P., & Ito, G. (2019). Multi-Channel Seismic Shot Data from the Hawaii-Emperor seamount chain acquired during Langseth cruise MGL1806 (2018). *MGDS*. doi:10.1594/IEDA/324706

Shillington, D. J., Bécel, A., Nedimović, M. R., Kuehn, H., Webb, S. C., Abers, G. A., . . . Mattei-Salicrup, G. A. (2015). Link between plate fabric, hydration and subduction zone seismicity in Alaska. *Nature Geoscience, 8*(12), 961-964.

Song, H., Chen, J., Pinheiro, L. M., Ruddick, B., Fan, W., Gong, Y., & Zhang, K. (2021). Progress and prospects of seismic oceanography. *Deep Sea Research Part I: Oceanographic Research Papers*, 103631.

St. Laurent, L., & Garrett, C. (2002). The role of internal tides in mixing the deep ocean. *Journal of Physical Oceanography, 32*(10), 2882-2899.

St. Laurent, L. C., Toole, J. M., & Schmitt, R. W. (2001). Buoyancy forcing by turbulence above rough topography in the abyssal Brazil Basin. *Journal of Physical Oceanography, 31*(12), 3476-3495.

Tang, Q., Gulick, S. P., Sun, J., Sun, L., & Jing, Z. (2020). Submesoscale features and turbulent mixing of an oblique anticyclonic eddy in the Gulf of Alaska investigated by marine seismic survey data. *Journal of Geophysical Research: Oceans, 125*(1), e2019JC015393.

Tang, Q., Jing, Z., Li, J., & Sun, J. (2022). Enhanced diapycnal mixing in the deep ocean around the island of Taiwan. *Journal of Geophysical Research: Oceans, 127*(5), e2021JC018034.

Tang, Q., Jing, Z., Lin, J., & Sun, J. (2021). Diapycnal Mixing in the Subthermocline of the Mariana Ridge from High-Resolution Seismic Images. *Journal of Physical Oceanography, 51*(4), 1283-1300.

Vic, C., Naveira Garabato, A. C., Green, J., Waterhouse, A. F., Zhao, Z., Melet, A., . . . Stephenson, G. R. (2019). Deep-ocean mixing driven by small-scale internal tides. *Nature communications, 10*(1), 1-9.

Waterhouse, A. F., MacKinnon, J. A., Nash, J. D., Alford, M. H., Kunze, E., Simmons, H. L., . . . Pinkel, R. (2014). Global patterns of diapycnal mixing from measurements of the turbulent dissipation rate. *Journal of Physical Oceanography, 44*(7), 1854-1872.

Watts, A., Grevemeyer, I., Shillington, D., Dunn, R., Boston, B., & Gómez de La Peña, L. (2021). Seismic structure, gravity anomalies and flexure along the Emperor Seamount chain. *Journal of Geophysical Research: Solid Earth, 126*(3), e2020JB021109.

Wei, J., Gunn, K. L., & Reece, R. (2022). Mid-Ocean Ridge and Storm Enhanced Mixing in the Central South Atlantic Thermocline. *Frontiers in Marine Science, 8*, 771973.

Whalen, C., Talley, L., & MacKinnon, J. (2012). Spatial and temporal variability of global ocean mixing inferred from Argo profiles. *Geophysical Research Letters, 39*(18).

Whalen, C. B. (2021). Best practices for comparing ocean turbulence measurements across spatiotemporal scales. *Journal of Atmospheric and Oceanic Technology, 38*(4), 837-841.

Whalen, C. B., De Lavergne, C., Naveira Garabato, A. C., Klymak, J. M., Mackinnon, J. A., & Sheen, K. L. (2020). Internal wave-driven mixing: Governing processes and consequences for climate. *Nature Reviews Earth & Environment, 1*(11), 606-621.

Whalen, C. B., MacKinnon, J. A., & Talley, L. D. (2018). Large-scale impacts of the mesoscale environment on mixing from wind-driven internal waves. *Nature Geoscience, 11*(11), 842-847.

Yang, S., Song, H., Coakley, B., & Zhang, K. (2023). Enhanced Mixing at the Edges of Mesoscale Eddies Observed From High‐Resolution Seismic Data in the Western Arctic Ocean. *Journal of Geophysical Research: Oceans, 128*(10), e2023JC019964.

Yilmaz, Ö. (2001). *Seismic data analysis: Processing, inversion, and interpretation of seismic data*: Society of exploration geophysicists.

Zhang, K., Zuo, W., Chen, Y., Meng, D., & Zhang, L. (2017). Beyond a gaussian denoiser: Residual learning of deep cnn for image denoising. *IEEE Transactions on Image Processing, 26*(7), 3142-3155.

Zhao, Z., Alford, M. H., Girton, J. B., Rainville, L., & Simmons, H. L. (2016). Global observations of open-ocean mode-1 M2 internal tides. *Journal of Physical Oceanography, 46*(6), 1657-1684.